Hydraulic fracturing process in rocks – small-scale simulations with a novel fully coupled DEM/CFD-based thermo-hydro-mechanical approach

M. Krzaczek , J. Tejchman [*]

Gdansk University of Technology, Faculty of Civil and Environmental Engineering 80-233 Gdańsk, Narutowicza 11/12, Poland

ABSTRACT

In the paper, a two-dimensional (2D) numerical simulation of a small-scale hydraulic fracturing process in rock specimens possessing a single injection slot was conducted. A unique DEM/CFD-based pore-scale thermal-hydro-mechanical (THM) model was used to simulate two-phase laminar fluid flow (water and gas) with heat transfer in non-saturated porous materials with low porosity. Using a DEM fully coupled with CFD (based on a fluid flow network composed of channels in a continuous domain between discrete elements) and heat transfer at the mesoscale, a series of numerical calculations for small cohesive granular specimens of simplified spherical mesostructure with one injection slot were carried out. Plane strain compression conditions were assumed. Both the fluid (diffusion and advection) and bonded particles (conduction) were involved in heat transfer. The impacts of the fluid's dynamic viscosity, gas phase content, and temperature difference between the rock matrix and the fluid injection on the process of hydraulic fracture initiation and propagation were all examined in-depth. It was discovered that those effects were all of great significance to the behaviour of a single hydraulic fracture.

1. Introduction

1.1. Hydraulic fracturing

Hydraulic fracturing (HF) is a major technique (developed steadily since 1947) for increasing the productivity of petroleum, gas, or heat in low-permeability rock formations [1–13]. HF enables the economic extraction of petroleum/gas/heat from rocks that have a permeability of less than 10^{-16} m^2 (e.g. the shale permeability usually ranges from 10^{-21} – 10^{-19} m^2; it is very low due to the small grain size [8]). By pumping a significant amount of pressurized fluid at a pressure of about 70 MPa into a wellbore, this technique fractures rocks at a target depth of roughly 2–6 km, causing either cracks to form in the deep-rock formations or strengthening the connectivity of the pre-existing fracture network, allowing natural gas, petroleum, and heat to flow more freely by exceeding the pressure gradient of rocks [1–3]. This technology uses horizontal wellbores because they offer a far larger exposure to a formation than traditional vertical wellbores. Clusters of shaped explosive charges puncture the steel casing of a horizontal part of the wellbore with an inner diameter of about 80 mm. With a spacing of roughly 10–20 m, the perforations serve as inlets for pressured fracturing water. Typically, horizontal boreholes are a few kilometers long and spaced roughly 500 m apart [8]. Each one is broken into five segments,

Nomenclature

A	area
$\overrightarrow{A}$	area normal vector
c_p	specific heat
C	cohesive contact stress
d	particle diameter
d_{50}	mean particle diameter
D	specimen diameter
e	edge length between two adjacent triangles
E	energy
E_c	modulus of elasticity of particle contact
$\overrightarrow{F}_{damp}^{k}$	dampened contact force vector
$\overrightarrow{F}_n$	normal contact force vector
$\overrightarrow{F}_s$	tangential contact force vector
F_{max}^{s}	critical cohesive contact force
F_{min}^{n}	minimum tensile force
h	hydraulic aperture of channels
h	enthalpy
h_{inf}	hydraulic aperture for infinite normal stress
h_0	hydraulic aperture for zero normal stress
K_n	normal contact stiffness
K_s	tangential contact stiffness
l	fracture length
L	channel length
M	mass fluid flow rate
$\overrightarrow{N}$	unit normal vector at contact point
p	micro-porosity
P	fluid pressure
Q	volumetric flow rate
R	particle radius, universal gas constant
Re	Reynolds number
S_h	energy source
t	time
T	tensile normal contact stress, temperature
u_i	interfacial velocity
u	velocity vector
U	overlap between discrete elements
w	molecular weight
$\overrightarrow{v}$	velocity vector
V	volume
$V_{q/p}$	molar volume of liquid/gas phase
α_d	damping parameter
α_{exp}	thermal expansion coefficient
α_p	gas phase volume fraction
α_q	liquid phase volume fraction
β	aperture coefficient
γ	fluid reduction factor
κ	permeability coefficient
λ	thermal fluid/solid conductivity
μ	dynamic fluid viscosity
μ_c	Coulomb inter-particle friction angle
ν_c	Poisson's ratio of particle contact
ρ	fluid density
ρ_{eff}	effective fluid density
σ	normal stress
τ	shear stress
ω	angle
$\omega_{q/p}$	acentric factor of liquid/gas phase

followed by five to nine fracturing stages that are each roughly 70 m long, 150 m deep, and 500 m broad [8]. A slurry of water, proppant (sand), and chemical additives called hydraulic fracturing fluid is frequently used to open and enlarge cracks in rock formations. Small grains of hydraulic fracturing proppants keep the cracks open when the hydraulic pressure is released from the well. A slurry blender, one or more high-pressure, high-volume fracturing pumps, and a monitoring device typically make up hydraulic fracturing equipment. Pumps push the fracturing fluid through the perforations and into the shale layer under the pressure of roughly 25–60 MPa. At a continuous rate of around 2 m^3/s, fluid is injected. The tight shale gas layer typically lies 3 km below the surface and has a thickness of 20–150 m. Its age ranges from 100 to 300 million years. The gas extraction from deep shale layers (20–150 m in thickness) is now at about 5–15% [8,9]. This percentage is still very high in the face of extremely low shale permeability. It means that during HF the rock permeability must be significantly increased by both opening already-closed cracks (that follow the rock joint and slide fault network) and initiating brand-new hydraulic cracks in intact shales. The overall permeability is enhanced by dense networks of branched cracks that HF creates, whose spacing and opening width are sufficient (cracks have a spacing of about 0.1 m [10,13]). Since the precise geometry of subsurface cracks is still unknown, most of the understanding of the fracturing process is empirical. Different hydraulic fracture patterns are caused by conditions for which there is no control. The laboratory tests described in [12] demonstrated a significant influence of injection rates and fluid viscosities on fracture branching patterns. According to the notion put forward in [14], high gas pressure may result in the formation of extensive cracked rock networks. In macropores of rocks, gas exists as a real gas, whereas in micro- and nanopores, it exists as a quasi-liquid (in an adsorbed state). In micro- and nanopores, the gas has significant internal energy. Similar to the rock-gas outburst in coal mines, gas desorption from an adsorptive phase occurs during hydraulic fracturing when the pore pressure abruptly decreases, greatly increasing the volume of cracks. Creep due to confining stress reduces the gas permeability by tending to close any existing flow nanochannels [9]. Testing the propagation of fracture networks in situ and at the laboratory scale is difficult. Therefore, it is essential to construct a realistic numerical model to comprehend and describe the rock crack phenomenon during the development of hydraulic fracturing and to optimize it for enhancing a gas extraction (e.g. by changing the pumping rate/cycles and fluid viscosity) for overcoming partly the shortages of experimental methods. Numerical simulation studies are, thus, necessary to increase the efficiency of HF [10,13]. Nevertheless, there are a number of challenging problems that must be solved in simulations, including e.g. coupling strategy between the solid and fluid domain and remeshing process (data transfer from the old mesh to the new mesh) induced by significant solid deformation caused by fluid pressure, multiphase flow, and thermal strains.

2. Research aims

The current paper aims to quantitatively illustrate the effect of the injected fluid temperature, the fluid dynamic viscosity (dependent upon temperature), and the gas content in macro-pores on the evolution of a hydraulic fracture, fluid/gas pressures, and velocities during a small-scale hydraulic fracturing process in rock specimens under two-dimensional (2D) conditions (the 3D DEM/ CFD model is still under construction). For non-saturated porous materials with very low porosity, a unique DEM/CFD-based thermal-hydro-mechanical technique of pressurized fracturing laminar viscous fluid flow of a variable temperature containing liquid and gas was devised [15]. Heat transfer involved both the fluid (diffusion and advection) and cohesive granular particles (conduction). Numerical 2D THM mesoscopic computations were performed utilizing a DEM along with the fluid flow and heat transfer. By using discrete spherical elements interacting through elastic-brittle normal contacts that could break to cause fractures, DEM was used to depict the mechanical behaviour of the rock mass. Laminar viscous two-phase (water and gas) fracturing fluid flow through pores and cracks in a continuous domain between the spherical discrete elements was described using CFD (where a flow network made up of channels was adopted). Small-size cohesive granular specimens imitating rock under plane strain compression were subjected to THM calculations in non-isothermal settings. In the first estimate, the rock specimen consisted of spheres of different diameters with no pre-existing micro-cracks/faults/bedding layers and with a single injection slot. The effects of the temperature difference between the rock matrix and the fluid being injected, the fluid's dynamic viscosity, and the amount of gas present in the rock matrix on the initiation and spread of a single hydraulic fracture were the next factors to be examined in-depth in a series of small-scale hydraulic fracturing simulations.

This article is a follow-up to the authors' earlier small-size mesoscopic numerical studies on hydraulic fracturing in rock segments [16,17], which utilized and extensively discussed a 2D fully coupled DEM/CFD technique without heat transfer. The technique was based on a fluid flow network of channels in the continuous domain between particles. It assumed one or two injection slots, various pre-existing macro-cracks, and bedding layers to account for one- or two-phase fracturing laminar viscous fluid flow in unsaturated rock segments. Without any extra assumptions, the fracture branching spontaneously appeared in HF simulations [17]. The coupled DEM/CFD technique without heat transfer was validated with comprehensive 3D CFD calculations utilizing the Reynolds-averaged Navier-Stokes equations in the continuous domain between particles [18,19]. Modelling hydraulic/capillary flow in unsaturated mortars and concretes was also carried out using this coupled DEM/CFD approach without heat transfer [20]. Here, a novel mathematical THM model was applied [15] that took additionally into account heat transfer in both rock and fracturing fluid.

2.1. Literature overview

The literature review of thermal–hydraulic-mechanical models was given in [15]. Continuous [21–27], discrete [28–33], and lattice Boltzmann methods (LBMs) [34,35] approaches have been widely used in THM models. Continuum modelling techniques are attractive for large-scale applications. However, they possess significant computational and continuity limitations when used with discontinuous and highly deformable media, such as packed or fluidized beds and fractured bonded granular porous materials. In

addition, the numerical generation of fine meshes in porous materials with low porosity (less than about 15%), such as concrete or rocks, is not easy. The issue is greatly exacerbated when simulating crack initiation and propagation in porous materials with low porosity (e.g. concrete or rocks). Discrete modelling approaches, such as the discrete element method (DEM) and lattice element models (LEM) [36] are effective in the mesoscopic modelling of cracks in bonded particulate materials with very low porosities. The concept of lattice elements [36] is very similar to the discrete element method (DEM) with cohesion, in which rigid particles are kept together by cohesive forces (simulated by beams). Since DEM models more correctly depict mesostructure and contact forces, they are more realistic than lattice models in describing a fracture process in engineering materials. Usually, the lattice models' responses are too brittle. They are also exclusively intended for static simulations. DEM models are therefore frequently employed in conjunction with fluid flow and heat transfer models.

The 3D fluid flow in a continuous domain between particles in DEM can be simulated with a variety of numerical techniques. Direct numerical simulations and co-simulations are the two basic ways for coupling DEM with fully resolved methods. In the direct numerical simulations method, the complexity of the fluid domain geometry is highly time-consuming to generate a fine enough mesh automatically. In addition, since the fluid domain topology may also strongly vary (e.g. during crack initiation and propagation), it is necessary to renew the mesh and transfer the numerical findings from the old mesh to the new mesh. As a result, there are significant numerical issues that arise when using traditional numerical methods (such as FEM, FVM, LBM, etc), which extend the acceptable computation window even for supercomputers. A significant flaw in the co-simulations used to couple DEM with traditional numerical techniques is that the particle volume must be substantially smaller than the grid cell volume of the discretized continuum. The DEM specimens cannot satisfy this condition when the porosity is extremely low. To decrease computing costs and overcome numerical restrictions when utilizing DEM to THM processes in very dense fluid-particle systems with very low porosity (even below 5%), e.g. shale rocks, the fluid flow and heat transfer models must be simplified. Recent DEM-based THM models separate fluid flow within reservoirs (pores, macro-pores, pre-existing cracks, etc.) from that between reservoirs [37–40]. The fluid flow regime in the reservoirs is stationary or almost stagnant, however, the fluid flow between the reservoirs is laminar, making it possible to estimate the mass flow rates at the edges of the reservoirs. To predict mass flow rates, a Poiseuille flow model in pipes or between two parallel plates is typically used. The models presuppose a single-phase barotropic flow of a pure liquid or mixture (without tracking phase fractions). In this technique, several heat transfer models are integrated with DEM-CFD models. Tomac and Gutierrez [32] calculated the energy conservation equation for each reservoir (cell) volume. The chosen energy conservation equation dealt with energy transfer in the laminar flow of an incompressible fluid. Caulk et al. [33] proposed a more advanced 3D DEM-based THM model based on the pore-scale finite volume (PFV) scheme which was first put forth by Chareyre et al. [42] and later extended by Scholtès et al. [43] for up-scaling compressible viscous flow. In contrast to other approaches used in unresolved CFD-DEM models, Che et al.'s [44] method can more precisely forecast the fluid-particle interacting force for a polydisperse particle system. The unresolved flow CFD-DEM methodology is still the foundation of this improved method, which is only applicable to issues where the cell volume is significantly larger than the total volume of particles, or to materials with extremely high porosity (over 30%). The Navier-Stokes equations are solved in a porous form in the unresolved CFD-DEM technique. For very low porosities (less than 5%), the method suggested by Che et al. [44] resolves certain issues, but the drawbacks of this strategy continue to be problematic. A limitation of CFD-DEM coupling methods is the difficulty for applications to industrial-scale problems due to the huge time of computation. A 3D numerical FEM/CFD model of small-scale hydraulic fracturing was recently proposed [13]. By beforehand constructing a network of vertical and horizontal channels with various initial Biot effective stress coefficients, the crack branching was numerically enforced.

The 2D DEM/CFD-based THM mesoscopic modeling method for heat transfer and fluid flow in non-saturated porous materials with very low porosity, presented in the current study is novel and offers pronounced benefits over other approaches that have been proposed in the literature (e.g. [45–53]). To simulate THM processes during hydraulic fracturing, coupled DEM/CFD THM models of multi-phase supercritical fluid flow in unsaturated rocks are not available. Here are a few of the benefits of the model used [15]:

1. Fluid/gas fractions in pores are properly tracked by accounting for the variable geometry, size, and position of pores.

2. A powerful technique for autonomously meshing and remeshing particle and fluid domains is developed to account for changes in their geometry and topology.

3. To create a virtual fluid flow network (VPN) and solve the energy conservation equation, coarse meshes of solid and liquid domains are used.

4. On a very coarse mesh of cells, FVM is used to solve the energy conservation equation in both domains.

5. Fluid flow is two-phase and contains both fluid and gas.

6. To account for supercritical fluid movement, a modified Peng-Robinson equation of state is applied for both fluid phases.

7. Variable heat fields in both pores and particles are computed.

8. To accurately measure fluid volume changes over time, virtual thermal deformation of discrete parts is tracked.

The results of the THM simulation, which are shown in the paper, replicate the initial stage of hydraulic fracturing without accounting for the existence of proppant particles. Only a hydraulic fracture's initiation and spread are addressed in the first stage. The dynamic viscosity of the injected fluid indirectly accounts for the proppant. The presence of proppant particles will, however, be directly replicated in simulations of the second stage of hydraulic fracturing (the proposed THM model reproduces this occurrence with ease).

The current paper is structured as follows. Following the introduction in Section 1, Section 2 offers a mathematical model of the DEM/CFD-based linked thermal-hydro-mechanical technique. The input data for THM simulations are described in Section 3. A series of numerical simulation results on hydraulic fracturing in rock specimens are shown in Section 4. Finally, Section 5 includes a few closing notes. The authors incorporated the THM model into the YADE open-source software package [54,55].
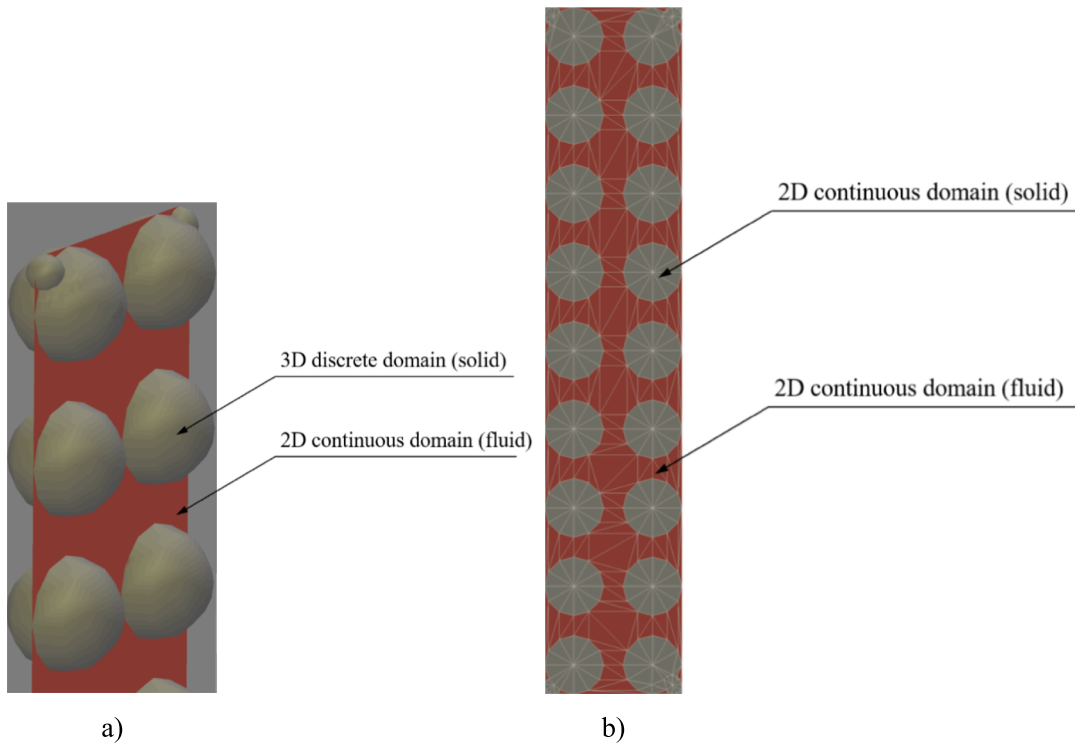
Fig.1. Two domains coexisting in one physical system: a) co-existing domains before projection and discretization and b) solid and fluid domains after discrete element projection and discretisation (fluid domain is in red colour and solid domain is in grey colour) [15]. (For interpretation of the references to colour in this figure legend, the reader is referred to the web version of this article.)

3. Two-dimensional DEM/CFD-based THM model

The THM model was described in-depth in [15]. Section 2 solely includes the most important information regarding the model for the sake of clarity.

The discrete (solid) and continuous (fluid) domains coexist in a physical system, according to the underlying theory behind the THM model. Discrete 3D elements (spheres) are initially arranged in a single layer within the solid domain (Fig. 1a). Next, the components are projected onto the plane to create circles (Fig. 1b). Heat transfer equations are solved in both the 2D fluid and solid continuous domains, and fluid flow equations are solved in the 2D fluid continuous domain (red colour in Fig. 1b) (red and grey colours in Fig. 1b).

3.1. DEM for cohesive-frictional materials

The 3D explicit discrete element open code YADE [54,55] was used to perform DEM simulations [15], which allows for overlap between two touched bodies (soft-particle model). Particles in DEM interact with one another during translational and rotational motions utilizing a contact law and Newton's second law of motion with an explicit time-stepping approach [56]. Since DEM takes into account inertial forces, it is a dynamic technique. The model proposes a cohesive bond at the grain contact with a brittle failure below the critical normal tensile force. Shear cohesion failure under typical compression leads to contact slip and sliding, which are governed by the Coulomb friction law. Fig. 2 illustrates the mechanical response of DEM. The following are the DEM equations

$$\vec{F}_n = K_n U \vec{N} \tag{1}$$

$$\vec{F}_s = \vec{F}_{s,prev} + K_s \Delta \vec{X}_s, \tag{2}$$

$$K_n = E_c \frac{2R_A R_B}{R_A + R_B} \text{ and } K_s = v_c E_c \frac{2R_A R_B}{R_A + R_B}, \tag{3}$$

$$\left\| \vec{F}_s \right\| - F_{max}^s - \left\| \vec{F}_n \right\| \times \tan\mu_c \leq 0 \text{ (before contact breakage)}, \tag{4}$$
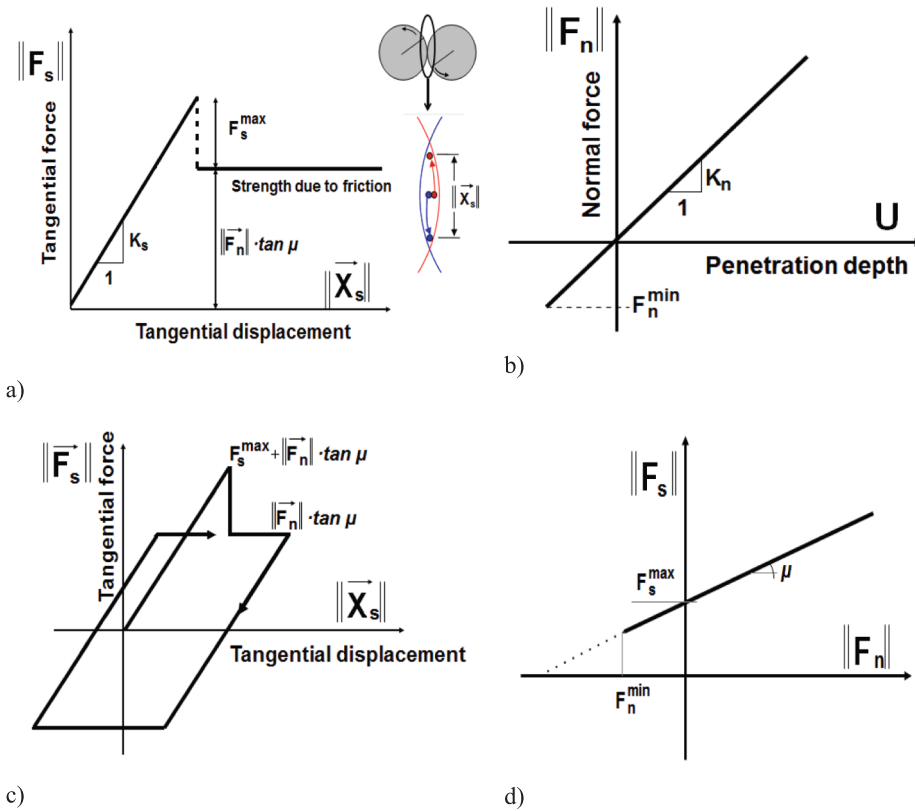
Fig.2. Mechanical response of DEM: a) tangential contact model, b) normal contact model, c) loading and unloading path in tangential contact model and d) modified Mohr-Coulomb model [16,17,55].

$$\left\| \overrightarrow{F}_s \right\| - \| \overrightarrow{F}_n \| \times \tan\mu_c \leq 0 \text{ (after contact breakage)},$$ (5)

$$F_{max}^s = CR^2 \text{ and } F_{min}^n = TR^2,$$ (6)

$$\overrightarrow{F}_{damp}^k = \overrightarrow{F}^k - \alpha_d \bullet \text{sgn}\left(\overrightarrow{v}_p^k \right) \overrightarrow{F}^k$$ (7)

where $\overrightarrow{F}_n$ - the normal contact force, U - the overlap between discrete elements, $\overrightarrow{N}$ - the unit normal vector at the contact point, $\overrightarrow{F}_s$ - the tangential contact force, $\overrightarrow{F}_{s,prev}$ - the tangential contact force in the previous iteration, $\overrightarrow{X}_s$ - the relative tangential displacement increment, K_n - the normal contact stiffness, K_s - the tangential contact stiffness, E_c - the elastic modulus of the particle contact, v_c - the Poisson's ratio of particle contact, R - the particle radius, R_A and R_B contacting particle radii, μ_c - the Coulomb inter-particle friction angle, F_{max}^s - the critical cohesive contact force, F_{min}^n - the minimum tensile force, C - the cohesion at the contact (maximum shear stress at zero pressure), and T - the tensile strength of the contact, $\overrightarrow{F}_{damp}^k$ - the dampened contact force, $\overrightarrow{F}^k$ and $\overrightarrow{v}_p^k$ - k^{th} - the components of the residual force and translational particle velocity v_p and α_d - the positive damping coefficient smaller than 1 (sgn($\bullet$) that returns the sign of the kth component of velocity). To accelerate convergence in quasi-static simulations, non-viscous damping was used [57] (Eq.7).

In pure DEM that does not include partial differential equations, regularization is not required. Thus, a discrete equation system is immediately obtained by this method and is well-posed. Contrarily, continuum models require regularization because they are based on partial differential equations that change their type when softening effects brought on by damage or strain localization appear (this results in ill-posed boundary value problems that result in mesh-dependent, physically meaningless finite element results) [58–60]. When the size and direction of the mesh used for discretization are changed, the predictions of the finite element simulations alter dramatically. To retain well-posedness and remove mesh dependence, continuum models must be improved by introducing a characteristic length of microstructure employing gradient, viscous, or non-local terms [58–60].

For DEM simulations, the following material constants are necessary: E_c, v_c, μ_c, C, and T. The constants R, ρ (mass density) and α_d are also required. To accurately model the failure mode of specimens (brittle or quasi-brittle), the distribution of shear and tensile cracks, and the relationship between the uniaxial compressive and tensile strength, one must consider the ratio C/T [61].

The process of running a number of DEM simulations and comparing the results to experimental data from straightforward tests,
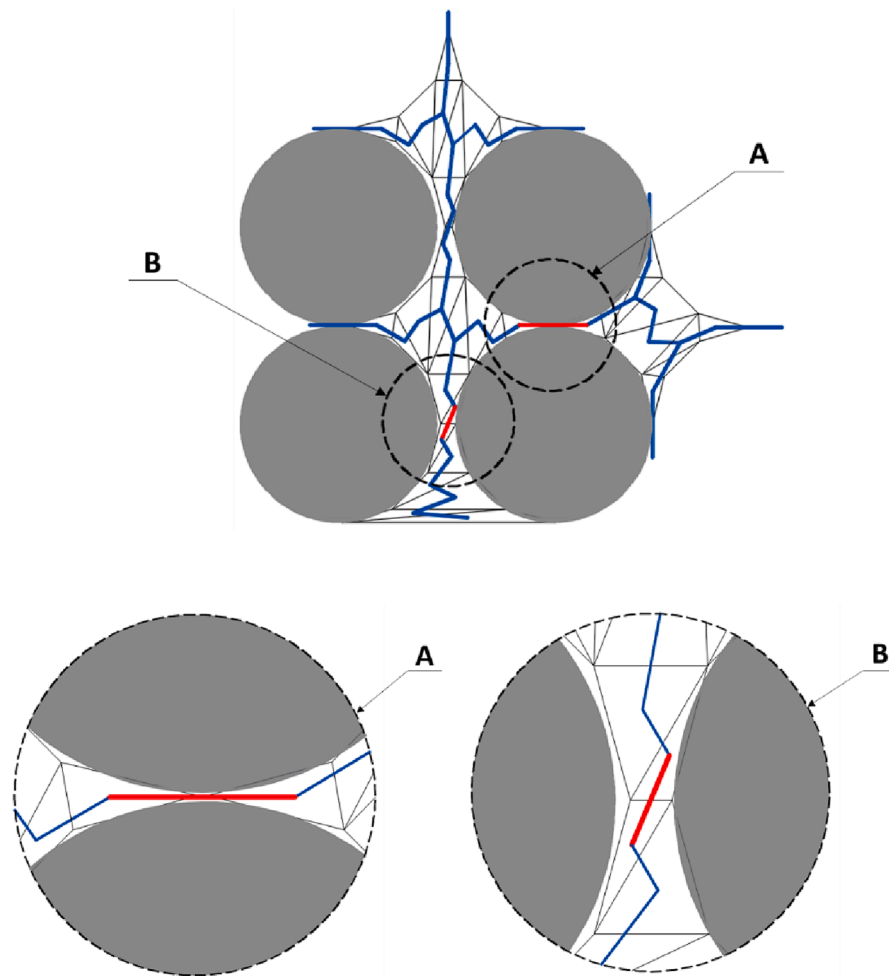
Fig.3. Fluid flow network in rock matrix with triangular discretization of pores (in blue): A) actual channel type 'S2S' (red colour) and B) artificial channel type 'T2T' (red colour) [16]. (For interpretation of the references to colour in this figure legend, the reader is referred to the web version of this article.)

such as uniaxial compression [62], triaxial compression, and simple shear, is typically used to determine the material constants. The damping factor was consistently set to $\alpha_d = 0.08$. The results are unaffected by the loading velocity v for this value [62]. If a cohesive joint between two spheres (Eg.6) vanishes after crossing a critical threshold, damage is sustained. If any contacts between spheres are to resume after failure, the cohesion does not appear more (Eq.5). The DEM model does not account for material softening. Bond damage in tension is the crucial micro-scale mechanism for damage in the pre-failure regime, despite the fact that bonds can also be damaged through shear. In DEM, an arbitrary micro-porosity may be attained due to the possibility of particle overlap. The fracture is prevented from spreading through the aggregate, i.e., the particle breaking is ignored. By taking into consideration shear localization and fracture, the model was successfully employed by the authors to describe the behaviour of several engineering materials with a granular structure, primarily granular materials [63–66], concrete materials [67–72], and rocks [61]. This issue may be easily taken into account in DEM simulations, although the computation time will be much increased.

The primary goal of the proposed DEM-based THM model is to investigate physical phenomena at the mesoscale while taking into account the actual mesostructure of rocks. Due to calculating time constraints, it cannot be used for extensive rock regions. However, macroscale continuum models that consider larger rock sections may take into account the results of mesoscale improved simulations. DEM is typically not scalable. There are, of course, some up-scaling techniques used with DEMs, such as mass/density/gravity scaling or grain up-scaling (precise scaling of grains and coarse-graining). However, when strain localization occurs in rocks, those up-scaling techniques fail. The strain localization area is large enough to generate a significant stress redistribution in the structure and an accompanying energy release, which together contribute to a noticeable size effect. Since the size of the localized strain cannot be scaled because it depends on the initial and boundary conditions of the entire system, scaling is not feasible. It must be noted that enhanced continuum models enhanced by a characteristic length of mesostructure (related to the grain size) require very fine meshes to obtain mesh-independent results in the case of strain localization. For example, when using non-local models, the element size should not be greater than the double characteristic length ([73,74]).

3.2. Fluid flow model

The idea of a novel 2D fluid flow model using DEM, based on a channel network in a continuous was discussed in the earlier authors' papers [16–20]. In the model, fluid flow is simulated by assuming that each particle contact is an artificial flow channel (between two parallel plates in 2D or along a duct in 3D) and that these channels connect actual reservoirs in the granular medium (pores, pre-existing cracks, fractures) that store fluid pressures depending on the mass transported along channels from/to other reservoirs and volume changes of reservoirs. Since the material deformation (represented by discrete elements in DEM) changes the reservoir volume, the fluid density likewise varies since the fluid in reservoirs is compressible. The reservoirs only serve to store pressures as the fluid moves in channels. The fluid flow in all channels is defined by a simplified laminar flow of an incompressible fluid, unlike the compressible fluid model in reservoirs.

As compared to the original concept of a fluid flow network reported in [40–42], in addition to storing pressures, the reservoirs (pores, cracks, pre-existing cracks, etc.) stores also phase fractions, fluid densities, energy, and temperature in the present model. A continuity equation is used to calculate the density of fluid phases in reservoirs. By using the equation of state for each phase and assuming that all fluid phases have the same pressure, the fluid phase fractions in reservoirs are calculated (as in the Euler model of multi-phase flow). By resolving continuity and momentum equations for laminar flows of an incompressible fluid, the mass flow rate is determined in channels. The 2D mid-plane is projected with the 3D particles which are then discretized into 2D polygons [16]. A remeshing process discretizes the overlapping circles, establishes the contact lines, and eliminates the overlapping areas to obtain a more accurate distribution of pressures, fluid-phase fractions, and densities [16]. Each reservoir is discretized by triangles, called the Virtual Pores (VPs) (Fig. 3). The actual channel link the gravity centres of triangles. The spheres are subjected to all forces generated by pressure and shear stress. Based on the pressure and shear stress for the specimen's thickness equal to the maximum particle diameter, the forces are calculated. VPs store energy, temperature, and both fluid-phase fractions and densities in addition to accumulating pressure. The density change in a fluid phase, which generates pressure changes, is connected to the mass change in VPs. As a result, the equation for the conservation of momentum is disregarded in triangles, but the mass is still conserved throughout their entire volume.

Using an explicit formulation, this process is repeated for each VP in the VPN and each solid cell. The liquid and gas initially might exist in the rock matrix and pre-existing discontinuities. The Virtual Pore Network introduces two different types of channels [16] (Fig. 3): A) the channels between discrete elements of the rock matrix in contact (referred to as the 'S2S' channels) and B) the channels connecting together grid triangles in pores that are in contact with one another along a common edge (referred to as the 'T2T' channels). The distance between the gravity centers of consecutive grid triangles is believed to be the channel length. The fluid flows around the spheres in contact in three-dimensional conditions. However, there is no room for fluid flow in 2D problems. Consequently, the idea of virtual 'S2S' channels is introduced [16]. According to a modified empirical formula of Hökmark et al. [75], the hydraulic aperture h of the artificial channels 'S2S' is related to the normal stress at the particle contact:

$$h = \beta \left(h_{inf} + \left(h_0 - h_{inf} \right) e^{-1.5 \bullet 10^{-7} \sigma_n} \right) \tag{8}$$

where h_{inf} - the hydraulic aperture for the infinite normal stress, h_0 - the hydraulic aperture for the zero normal stress, σ_n - the effective normal stress at the particle contact and β - the aperture coefficient. The hydraulic aperture of the actual channels 'T2T' is directly related to the geometry of the adjacent triangles as

$$h = \gamma e \cos(90^\circ - \omega) \tag{9}$$

where e - the edge length between two adjacent triangles, ω - the angle between the edge with the length e and the centre line of the channel that connects two adjacent triangles and γ - the reduction factor, necessary to fit the fluid flow intensity to real complex fluid flow conditions in rocks. The reduction factor γ is determined in parametric studies to keep the maximum Reynolds number R_e along the main flow path always lower than the critical one for laminar flow [16]. The numerical algorithm is divided into five main stages [15]:

a) estimating the mass flow rate for each phase of fluid flowing through the cell faces (in channels surrounding VP) by using momentum and continuity equations,

b) computing the phase fractions and their densities in VP by using equations of state and continuity,

c) calculating pressure in VP by using the equation of state,

d) solving the energy conservation equation in fluid and solids, and,

e) updating material properties.

3.2.1. Mass flow rate in channels

Three flow regimes ate identified in the channels [17]: a) a single gas phase flow with a gas phase fraction α_p of 1, b) a single liquid phase flow with a liquid phase fraction α_q of 1, and c) two-phase flow (liquid and gas) with $0 < \alpha_q$ less than 1. According to a traditional lubrication theory [76], based on the Poiseuille flow rule [77], the fluid moves in channels through a thin film region separated by two closely spaced parallel plates for single-phase flow (flow regimes 'a' and 'b'). As a result, the single-phase flow along channels has a mass flow rate of
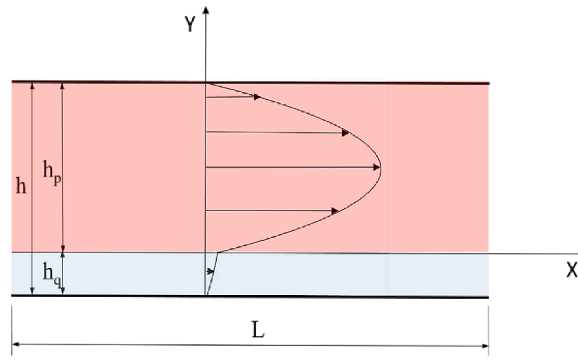
Fig.4. Two-layer fluid flow in channels 'S2S' and 'T2T' (h - channel aperture, L - channel length, 'q' - liquid and 'p' - gas) [17].

$$M_x = \rho \frac{h^3}{12\mu} \frac{P_i - P_j}{L} \tag{10}$$

where M_x - the mass fluid flow rate (per unit length) across the film thickness in the x-direction [kg/(m s)], L – the channel length, h - the hydraulic channel aperture (its perpendicular width) [m], ρ - the fluid density [kg/m³], t - the time [s], μ - the dynamic fluid (liquid or gas) viscosity [Pa s] and P - the fluid pressure [Pa] (P_i and P_j are the pressures in the adjacent VPs).

A two-phase fluid flow (flow regime 'c'), driven by a pressure gradient in adjacent VPs behaves similarly to a two-phase fluid flow of two immiscible and incompressible fluids in channels (Fig. 4). The liquid–gas interface is constant and parallel to the channel plates. The effects of gravity are ignored. In the undisturbed flow condition, the interface between the fluids, denoted by the symbols $j = q, p$ (q denotes the lower liquid phase, and p denotes the upper gas phase), is flat. The model provides for a plane-parallel solution under this supposition. The interface position is related to fractions of fluid phases in adjacent VPs while the volumetric flow rates of fluid phases are unknown. Continuity and momentum equations characterize the flow in each phase. The time and pressure are scaled by h_p/u_i and $\rho_p u_i^2$ (h_p - the height of the upper layer and u_i - the interfacial velocity). The dimensionless continuity and momentum equations are [78]

$$div\mathbf{u}_j = 0 \tag{11}$$

$$\frac{\partial \mathbf{u}_j}{\partial t} + \left(\mathbf{u}_j \bullet \nabla\right)\mathbf{u}_j = -\frac{\rho_q}{r\rho_j}\nabla p_j + \frac{1}{\mathrm{Re}_p}\frac{\rho_q}{r\rho_j}\frac{m\mu_j}{\mu_q}\Delta\mathbf{u}_j \tag{12}$$

where $\mathbf{u}_j = (u_j, v_j)$ and p_j are the velocity and pressure of the fluid phase j, ρ_j and μ_j are the corresponding density and dynamic viscosity. The Reynolds number is $\mathrm{Re}_p = \rho_p u_i h_p / \mu_p$ and the density and viscosity ratios are $r = \rho_q/\rho_p$ and $m = \mu_q/\mu_p$. In the dimensionless formulation, the lower and upper phases occupy the regions $-n_d \leq y \leq 0$ and $0 \leq y \leq 1$, where $n_d = h_q/h_p$. At the channel walls, the velocities satisfy the no-slip boundary condition

$$\mathbf{u}_q(y = -n_d) = 0 \text{ and } \mathbf{u}_p(y = 1) = 0. \tag{13}$$

The boundary conditions at the interface $y = 0$ require the continuity of velocities and tangential stresses [78]

$$\mathbf{u}_q(y = 0) = \mathbf{u}_p(y = 0) \tag{14}$$

and

$$\mu_q \left.\frac{\partial u_q}{\partial y}\right|_{y=0} = \mu_p \left.\frac{\partial u_p}{\partial y}\right|_{y=0} \tag{15}$$

The solution details are presented in [19]. Solving Eqs.11 and 12 with boundary conditions (Eqs.13–15), the mass flow rates $M_{q,x}$ and $M_{p,x}$ for both fluid phases are calculated (as well as the shear stress τ_{f0} at the channel surfaces for $y = -n_d$ and $y = 1$).

3.2.2. Fluid flow in virtual pores

The fluid pressure can reach e.g. 50–90 MPa during a hydraulic fracturing process. The gas phase exceeds the critical point and becomes a supercritical fluid under these conditions. For both fluid phases in VPs, the Peng-Robinson equation of state [79] is used for describing the fluid behaviour above the critical point at extremely high fluid pressures and temperatures [15]

$$P = \frac{RT}{\left(V_{q/p} - b_{q/p}\right)} - \frac{a_{q/p}}{\left(V_{q/p}^2 + 2b_{q/p}V_q - b_{q/p}^2\right)} \tag{16}$$

with

$$a_{q/p}(T) = a_{q/p,0}\left[1 + n_{q/p}\left(1 - \left(\frac{T_i^n}{T_{q/p,c}}\right)^{0.5}\right)\right]^2,$$ (17)

$$n_{q/p} = 0.37464 + 1.54226\omega_{q/p} - 0.26992\omega_{q/p}^2$$ (18)

$$a_{q/p,0} = a_{c,q/p}\beta(T),$$ (19)

$$a_{c,q/p} = \frac{0.457247R^2 T_{q/p,c}^2}{P_{q/p,c}},$$ (20)

$$b_{q/p} = \frac{0.07780RT_{q/p,c}}{P_{q/p,c}}$$ (21)

$$\beta = \left[1 + c_1\left(1 - T_r^{\frac{1}{2}}\right) + c_2\left(1 - T_r^{\frac{1}{2}}\right)^2 + c_3\left(1 - T_r^{\frac{1}{2}}\right)^3\right]^2,$$ (22)

where P is the pressure [Pa], R denotes the gas constant ($R = 8314,4598$ J/(kmol K)), $V_{q/p}$ is the molar volume of the liquid (q) and gas (p) fraction [m^3/kmol], T denotes the temperature [K], $T_{q/p,c}$ is the critical phase temperature [K], T_r denotes the reduced temperature $\frac{T}{T_c}$ [-], $P_{q/p,c}$ is the critical pressure of phase [Pa], $\omega_{q/p}$ is the acentric phase factor [-], and c_i are the constants (usually $c_1 = 1$, $c_2 = 0$ and $c_3 = 0$). The extra factors help connect vapor pressure data from highly polar liquids like water and methanol. Eqs. (17)–(22) provide a good fit for the vapor pressure, however predicting molar volumes can be very inaccurate (the prediction of saturated liquid molar quantities might deviate by l0-40% [80]). Peneloux and Rauzy [81] proposed an effective correction term

$$V_q^{corr} = V_q + s$$ (23)

where s is the small molar volume correction term that is component dependent; V_q is the molar volume predicted by Eq.16 and V_q^{corr} refers to the corrected molar volume. The value of s is negative for higher molecular weight non-polar and essentially for all polar substances. The molar volume correction term is 0 m^3/kmol and 0.0034 m^3/kmol for the gas phase and liquid phase (water), respectively. For each phase, the mass conservation equation is used. The mass transfer between phases and the grid velocity is ignored when there is no internal mass source. The discretized form of the mass conservation equation for the liquid phase is

$$\frac{\alpha_{q,i}^{n+1}\rho_{q,i}^{n+1}V_i^{n+1} - \alpha_{q,i}^n\rho_{q,i}^n V_i^n}{\Delta t} + \sum_f\left(\rho_{q,f}^n U_f^n \alpha_{q,f}^n\right) = 0$$ (24)

with

$$V_i^{n+1} = V_i^n + \frac{dV}{dt}\Delta t,$$ (25)

where f is the face (edge) number, U_f^n denotes the volume flux through the face [m^3/s], based on the average velocity in the channel, $\alpha_{q,f}^n$ is the face value of the fluid phase volume fraction [-], t is the time step [s], n denotes the time increment and i is the VP number [-]. The explicit formulation is used instead of an iterative solution of the transport equation during each time step since the volume fraction at the current time step is directly computed from known quantities at the previous time step. Similarly, the mass conservation equation for the gas phase is introduced. The product $\rho_q U_f^n \alpha_{q,f}^n$ in Eq.24 is the mass flow rate $M_{q,f}$ of the liquid phase flowing through the face f (edge of a triangle) of VP$_i$. The density of the liquid phase can be calculated by solving the mass conservation equation for both phases

$$\rho_{i,q}^{n+1} = \frac{\alpha_{q,i}^n\rho_{q,i}^n V_i^n + \Delta t\sum_f M_{q,f}}{\left(V_i^n + \Delta V_i\Delta t\right)\alpha_{q,i}^{n+1}}.$$ (26)

The density of the gas phase can also be computed in the same way. It should be noted that the molar volume $V_{(q/p)}$ is related to the gas density.

$$V_{i,p}^{n+1} = \frac{w_p}{\rho_{i,p}^{n+1}},$$ (27)

and to the liquid density

$$V_{i,q}^{n+1} = \frac{w_q}{\rho_{i,q}^{n+1}} - s.$$ (28)

Since the fluid phases shared the same pressure

$$\frac{RT_i^n}{\left(V_{i,p}^{n+1} - b_p\right)} - \frac{a_p}{\left(V_{i,p}^{n+1^2} + 2b_p V_{i,p}^{n+1} - b_p^2\right)} = \frac{RT_i^n}{\left(V_{i,q}^{n+1} - b_q\right)} - \frac{a_q}{\left(V_{i,q}^{n+1^2} + 2b_q V_{i,q}^{n+1} - b_q^2\right)},$$ (29)

the fluid phase fractions are computed. Inserting Eq.27 for the gas phase and Eq.28 for the liquid phase into Eq.29, a polynomial equation is obtained for the liquid fraction $\alpha_{q,i}^{n+1}$. The gas phase fraction is computed as $\alpha_{p,i}^{n+1} = 1 - \alpha_{q,i}^{n+1}$. Equation (16) is used to calculate the new pressure P_i^{n+1} in VP$_i$.

3.3. Heat transfer

Heat is transferred in both the fluid and solid domains [15]. In the case of the heat transfer in multi-phase fluid flow, the temperature is shared but enthalpy is transferred. The heat transfer model is simplified similarly to the fluid flow model. A homogeneous heat transfer model is assumed in multiphase flow (mass transfer between phases is not taken into account). The multiphase fluid is homogenized to a single-phase fluid. The effective fluid properties and velocity are calculated using volume averaging over the phases. The numerical solution uses the same coarse mesh (Fig. 1b) used in the fluid flow network to solve the governing equations.

The impact of applied external pressure on the thermal characteristics of rock is taken into account by the heat transfer model that is postulated in the study. Contrary to existing models, the proposed DEM-based THM model tracks the thermal deformations of particles (particle temperature distribution is non-uniform) and accurately determines the changes in pore volume that are transferred to CFD and influence the fluid's pressure and temperature.

3.3.1. Heat transfer in fluid

Homogenous heat transfer in multi-phase fluid flow is assumed [15]. The fluid is incompressible and homogeneous. The viscous dissipation of energy is not taken into account. The energy conservation equation is shared by all phases and is expressed in integral form

$$\int_V \frac{\partial \rho_{eff} E}{\partial t} dV + \oint \rho_{eff} \vec{v} E \bullet d\vec{A} = \oint \lambda_{eff} \nabla T \bullet d\vec{A} + \int_V S_h$$ (30)

where ρ_{eff} is the effective density of the fluid [kg/m³], E denotes the total energy [J], t is the time [s], $\vec{v}$ is velocity vector [m/s], T is the temperature [K], λ_{eff} denotes the effective thermal fluid conductivity [W/(mK)] and S_h represents the energy source term. The enthalpy h equation of state is

$$h = \int_{T_{ref}}^{T} c_p dT$$ (31)

where T_{ref} is the reference temperature [K] and c_p denotes the specific heat for constant pressure [J/(kg·K)]. The effective fluid properties and velocity are computed by the volume averaging over the phases

$$\rho_{eff} = \sum_{k=1}^{2} \alpha_k \rho_k$$ (32)

$$\vec{v}_{eff} = \frac{1}{\rho_{eff}} \sum_{k=1}^{2} \alpha_k \rho_k \vec{v}_k,$$ (33)

$$\lambda_{eff} = \sum_{k=1}^{2} \alpha_k \lambda_k$$ (34)

$$\mu_{eff} = \sum_{k=1}^{2} \alpha_k \mu_k$$ (35)

The specific heat capacity is assumed to be independent of composition and pressure

$$c_p = \sum_i \alpha_i c_{pi} = const$$ (36)

Equation (30) is applied to each fluid cell (triangle) in the computational domain. The finite volume method is used to solve Eq.30. The discretization of Eq.30 on a given cell produces

$$\frac{\partial \rho E}{\partial t} V + \sum_f^{N_{faces}} \rho_f \vec{v}_f E_f \bullet \vec{A}_f = \sum_f^{N_{faces}} \lambda_{eff} \nabla T_f \bullet \vec{A}_f + S_h V$$ (37)

where N_{faces} is the number of faces enclosing the cell, E_f is the value o E on the face f of the cell, T_f is the value of T on the face f, $\rho_f \vec{v}_f \bullet \vec{A}_f$ denotes the mass flux through the face f, $\vec{A}_f$ is the area vector of the face f, $|A| = |A_x \hat{i} + A_y \hat{j}|$ in 2D, ∇T_f denotes the gradient of
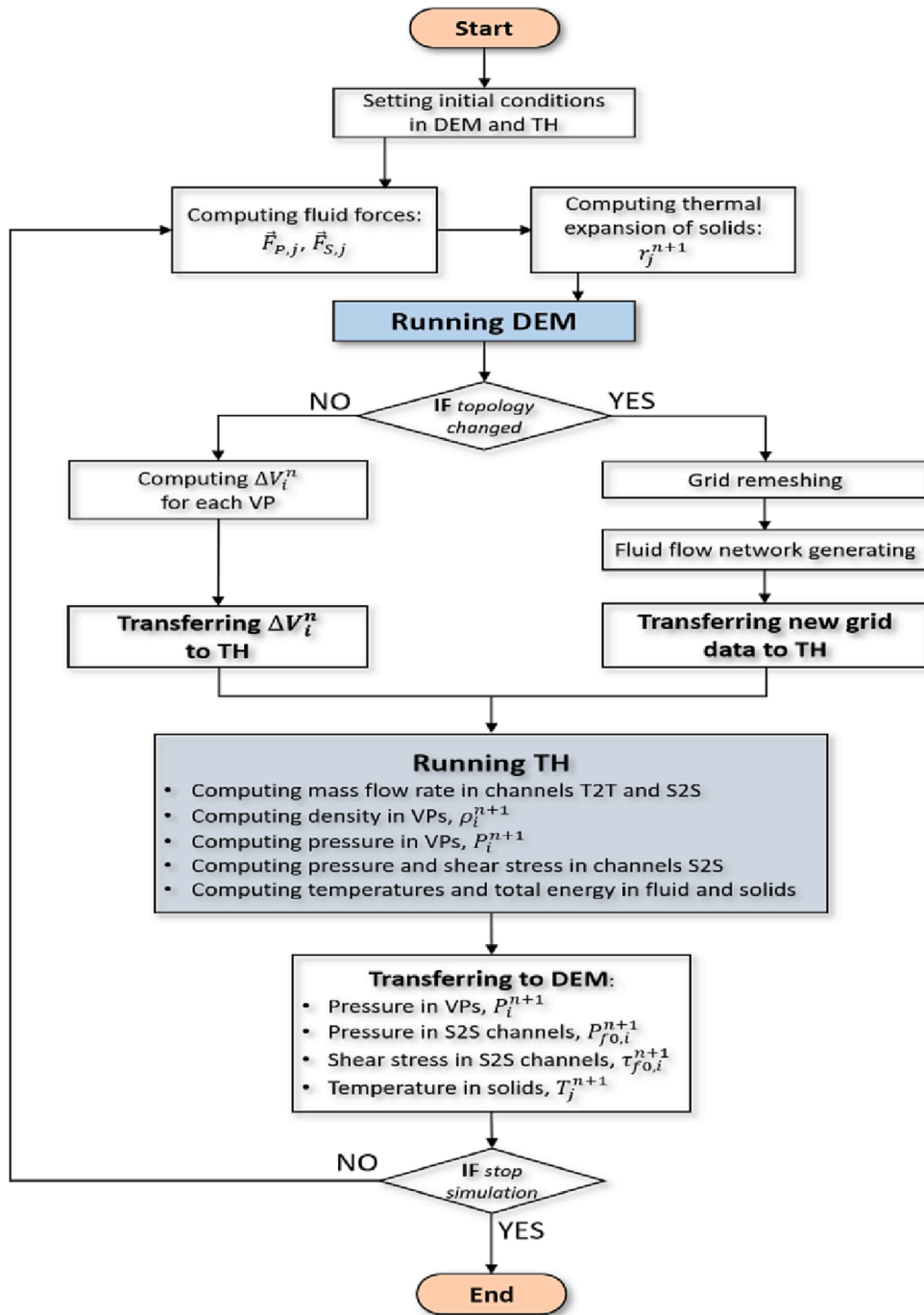
Fig.5. DEM-TH (thermo-hydro model) coupling schema ($\vec{F}_{P,j}$ - force converted from pressure in VP, $\vec{F}_{S,j}$ - force converted from shear stress in channels, ΔV_i^n - volume change in VP, T_j^{n+1} - temperature in cell j of solid domain, r_j^{n+1} - sphere radius and n - time increment) [15].

T at the face f and V is the cell volume. If the time derivative is discretized using backward differences, the first-order accurate temporal discretization is given by

$$\frac{\rho^{n+1}E^{n+1} - \rho^n E^n}{\Delta t}V + \sum_f^{N_{faces}} \rho_f^n \vec{v}_f^n E_f^n \bullet \vec{A}_f = \sum_f^{N_{faces}} \lambda_{eff} \nabla T_f^n \bullet \vec{A}_f + S_h V \tag{38}$$

where $n + 1$ is the value at the next time step $t + \Delta t$ and n is the value in the current time t. The energy conservation equation can be expressed in terms of temperature T by assuming that total energy E equals enthalpy h and applying the enthalpy equation of state to Eq.38

$$T^{n+1} = T_{ref} + \frac{c_{p,eff}^n \left(T^n - T_{ref}\right)}{c_{p,eff}^{n+1}} + \frac{\Delta t}{V \rho^n c_{p,eff}^{n+1}} \sum_f^{N_{faces}} \lambda_{eff} \nabla T_f^n \bullet \overrightarrow{A}_f - \frac{\Delta t}{V \rho^n c_{p,eff}^{n+1}} \sum_f^{N_{faces}} \rho_f^n \overrightarrow{v}_f^n c_{p,eff}^n \left(T_f^n - T_{ref}\right) \bullet \overrightarrow{A}_f + \frac{\Delta t}{\rho^{n+1} c_{p,eff}^{n+1}} S_h,$$

(39)

where S_h is related to the internal enthalpy source of the diffusive energy [W/m³] of heat transported by diffusion along the actual channel 'S2S'

$$S_h = -\lambda_{eff} \frac{T_i^n - T_j^n}{L_k} A_k \frac{1}{V},$$

(40)

where L_k is the length [m] of the channel'S2S' and A_k is the area of the channel cross-section [m²]. The total energy can be calculated using the enthalpy equation of state $E = c_p \left(T - T_{ref}\right)$ since total energy equals enthalpy. The finite volume method was employed to solve Eq. (39) [15].

3.3.2. Heat transfer in solid

The energy conservation equation has the following integral form if there is no convective energy transfer, no internal heat sources, and the constant density is in solid regions

$$\rho_s \int_V \frac{\partial E}{\partial t} \bullet dV = \oint \left(\lambda_s \nabla T\right) \bullet d\overrightarrow{A},$$

(48)

where E is the total energy, equal to enthalpy $h = \int_{T_{ref}}^T c_p dT$, ρ_s denotes the solid density [kg/m³], λ_s is the thermal conductivity of solid [W/(mK)], T_{ref} denotes the reference temperature and c_p is the specific heat in constant pressure. Equation (48) is applied to each cell (triangle) in the solid domain. The discretization of Eq.48 produces in a given cell

$$T^{n+1} = T^n + \frac{\Delta t}{V \rho_s c_p} \sum_f^{N_{faces}} \lambda_s \nabla T_f^n \bullet \overrightarrow{A}_f$$

(49)

The gradients and face values are computed in the same way as the fluid gradients and face values (Section 2.3). The total energy is calculated using the enthalpy state equation

$$E = c_p \left(T - T_{ref}\right)$$

(50)

The THM model was validated by comparing the numerical findings with the analytical solution for the classic 1D heat transfer problem (diffusion) in the cohesive granular bar specimen [15]. An almost perfect accordance was obtained.

The proposed DEM-based THM model employs a direct numerical simulation method, in contrast to existing models. To estimate the mass flow rates of the fluid across the mesh cell faces, the fluid flow model between particles was simplified to be based on the fluid flow network concept due to great computing efficiency. It is expected that the fluid flow in the channels will be laminar along smooth walls. In recent papers [18] and [19], we provided a comparison of the outcomes of the DEM-based THM model and the fully resolved CFD model. It was demonstrated that the turbulent kinetic energy and turbulent dissipation energy in a real hydraulic fracturing process are relatively low and may be disregarded in the simplified fluid flow model.

3.4. Coupling scheme

The discretization algorithm is based on the Alfa Shapes theory [82]. The volume changes (Eq.25) are transferred to CFD. When the topological features of the grid geometry change, the grid is automatically re-meshed [19]. Even though the mesh is coarse, the re-mesh procedure takes a relatively long computational time. Therefore, an algorithm that tracks configuration changes of discrete elements is developed and implemented in the model. This algorithm tracks displacements, overlaps, and size changes of discrete elements in each iteration (time increment). The re-meshing procedure runs when the configuration changes are large enough. The criterion for triggering the re-mesh procedure is based on the results of a parametric study. As a result, the repeated re-meshing procedure is run on average every several hundred or even several thousand iterations and slightly increases the total computation time. The calculation outputs (e.g., pressures, fluid fractions) are accurately converted from the old mesh to the new mesh, providing that the mass is a topological invariant [19]. Equation (29) is used to determine the new fluid phase fractions by using mass quantities rather than mass flow rates. In VPs, Eq.16 is utilized to calculate the new pressure after transformation. The two-way coupling scheme of DEM with CFD and heat transfer is presented in Fig. 5 and was explained in detail in [15].

4. Input data for 2D THM simulations

4.1. Calibration procedure

DEM and CFD were separately calibrated, based on mechanical 2D tests (DEM) and permeability 2D tests (CFD) [16]. A simple one-phase rock model composed of spheres of different diameters was chosen. The DEM model was calibrated to approximately describe

Table 1

Basic material constants assumed for rock matrix, fluid and gas in THM calculations of hydraulic fracturing for two-phase fluid flow.

Material constants for rock	Symbol	Value	Unit
modulus of elasticity of contact	E_C	3.36	[GPa]
Poisson's ratio of contact	v_c	0.35	[-]
cohesion at contact	C	170	[MPa]
tensile strength of contact	T	34	[MPa]
inter-particle friction angle	μ_c	18	[°]
mass density	ρ	2600	[kg/m^3]
initial porosity	p	5	[%]
specific heat	c_p	960.0	[J/(kg K)]
heat transfer coefficient	λ	3.5	[W/(m K)]
thermal expansion coefficient	α_{exp}	8.3·10^{-6}	[1/K]
Material constants for fluid			
dynamic viscosity	μ_q	4.06·10^{-4} or 2.44 10^{-4}	[Pa s]
reference pressure	P_0	0.1	[MPa]
density at reference pressure	ρ_0	977.36	[kg/m^3]
initial fluid volume fraction	α_q	1.0 or 0.8 or 0.6 or 0.4	[-]
specific heat	c_p	4187.0	[J/(kg K)]
heat transfer coefficient	λ	0.6	[W/(m K)]
molecular weight	w_q	18.01528	[kg/kmol]
critical temperature	T_c	647.096	[K]
critical pressure	P_c	22,064	[kPa]
accentric factor	ω_q	0.344	[-]
Material constants for gas			
dynamic viscosity	μ_p	2.0507·10^{-5}	[Pa s]
initial gas volume fraction	α_p	0 or 0.2 or 0.4 or 0.6	[-]
universal gas constant	R	8.3144598·10^{-4}	[J/(kmol K)]
specific heat	c_p	1006.0	[J/(kg K)]
heat transfer coefficient	λ	0.0262	[W/(m K)]
molecular weight	w_p	28.9647	[kg/kmol]
critical temperature	T_c	132.63	[K]
critical pressure	P_c	3786	[kPa]
accentric factor	ω_p	0.035	[-]
Fluid flow network parameters			
channel width	h_{inf}	2.5 • 10^{-8}	[m]
channel width	h_0	3.25 • 10^{-7}	[m]
aperture coefficient (Eq.8)	β	0.22	[-]
reduction factor (Eq.9)	γ	0.008	[-]

laboratory quasi-static test results for shale rock specimens during uniaxial compression and tension splitting [83]. A permeability test with a non-deformable fully saturated rock specimen was performed for CFD calibration. The specimens did not include any both pre-existing cracks or bedding layers. The spheres' diameter d was assumed arbitrarily; it was between 0.7 mm and 1.3 mm with a mean diameter of $d_{50} = 1$ mm. A quadratic specimen 100×100 mm^2 was assumed for uniaxial compression, and a circular specimen with a diameter of $D = 100$ mm was used for tension splitting (with about 10 000 spheres). In CFD simulation, a quadratic specimen of 10×10 mm^2 was chosen (with about 1500 spheres). The initial micro-porosity was assumed as $p = 5\%$ (corresponding to shale rocks [84]). The material constants in Table 1 (Section 3.2) were used in the analyses. The mechanical properties of specimens were not affected by the temperature.

4.1.1. Pure DEM simulations

The calculated maximum vertical compressive normal stress was $\sigma = 47$ MPa for the vertical normal strain $\varepsilon = 1\%$, and the maximum tensile splitting stress was $\sigma = 8$ MPa for the displacement of $u = 0.5$ mm; the values are in agreement with the experimental outcomes given in [82]. The numerical post-peak response of the rock specimen was too brittle in both cases due to some simplifications met (simple one-phase material, narrow particle diameter size range, 2D analyses, and a relatively small number of spheres [62]). The failure mode was characterized during uniaxial compression by the occurrence of a few almost vertical and skew macro-cracks, and during tension splitting by one vertical macro-crack [16] as in experiments [82].

4.1.2. Pure CFD calibration

The zero-flux conditions were imposed along the vertical walls and the pressures were prescribed along the horizontal walls of the specimen. The macroscopic permeability coefficient κ of the rock specimen was calculated with Darcy's law

$$\kappa = \frac{Q}{A} \mu_q \frac{L}{\Delta P} \tag{55}$$

where Q - the volumetric flow rate at the equilibrium, A - the specimen cross-section, L - the specimen height and ΔP - the pressure difference between the bottom and top wall. The cross-section A of specimen in the Eq.55 was defined as the product of the thickness
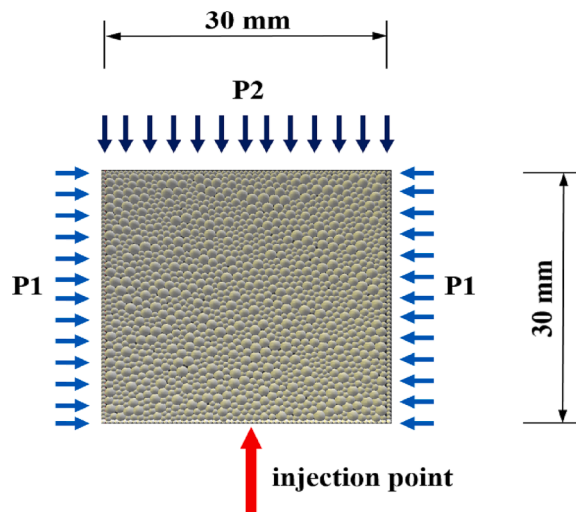
Fig.6. Geometry and boundary conditions of rock specimen subjected to hydraulic fracturing with one injection slot at bottom (P1 - horizontal pressure, P2 - vertical pressure, red arrow - injection point of fracturing fluid) [16,17]. (For interpretation of the references to colour in this figure legend, the reader is referred to the web version of this article.)

(largest diameter of spheres) and specimen width. A realistic one-dimensional fluid flow was obtained at the macroscopic level. The calculated permeability coefficient κ yielded the value of 1.09×10^{-21} m^2 for h_{inf}, h_0, γ, and β (Eqs.8 and 9) from Table 1 (Section 3.2), being in agreement with experimental values (e.g. [84]). The larger values of h_{inf}, h_0, γ, and β cause the permeability coefficient κ higher [20]. An arbitrary permeability coefficient may be, thus, assumed in numerical calculations.

4.2. Input data in THM simulations

The basic material constants for the fracturing fluid (liquid/gas) and rock matrix in the coupled DEM/THM calculations are given in Table 1. For simplicity, the specific heat and heat transfer coefficients of the supercritical fluid (originally gas phase) were adopted as the same as for the original gas phase.

A small-scale quadratic rock segment of 30 × 30 mm^2 (with 1500 spheres) was subjected to biaxial compression (Fig. 6). The pre-existing macro-pores were neglected. The micro-pores corresponded to the free space between spheres (the initial specimen's porosity was 5%). The diameter of spheres lay in the range of 0.7–1.3 mm (Section 3.1). Initial vertical (symbol 'P1' in Fig. 6) and horizontal (symbol 'P2′' in Fig. 6) normal stresses of 20 MPa were assumed to reproduce tectonic stresses at a depth. The rigid impermeable segment edges were assumed to be smooth (frictionless). All boundaries were free to move except the fixed bottom. One injection slot with a width of 0.5 mm was located at the bottom of the segment. The initial fluid pressure in the rock specimen was 15 MPa. The constant fluid pressure of 90 MPa was assumed at the injection point. This condition at the injection point is similar to a real hydraulic fracturing process in rocks which is controlled by changes in the flow rate to keep up the constant pressure. The DEM time step of 1×10^{-8} s was always assumed in the simulations [16]. The CFD time step was, however, about 2–10 times smaller [15–17]. The computations time of one simulation was about 10 days on a computer with two Intel Xeon Platinum processors 8280 (2.70 GHz). The computational cost of the simulation was relatively high because the existing DEM-based THM model was parallelized on threads only but not in a distributed mode (on cluster computer nodes) [15].

5. 2D THM simulation results

5.1. Effect of temperature difference

The influence of the temperature difference between the rock matrix and injected fluid on the process of initiation and propagation of a single hydraulic fracture above the injection point under non-isothermal conditions was investigated. The temperature of the injected fluid was constant and amounted to $T_f = 277.15$ K (4C) in all simulations carried out under non-isothermal conditions. Three different initial temperatures of the rock matrix were assumed: $Trm = 338.15$ K (65C), $Trm = 368.15$ K (95C), and $Trm = 408.15$ K (135 °C). Thus, the temperature difference between the injection point and the rock matrix was $\Delta T = 61$ K, $\Delta T = 91$ K, and $\Delta T = 131$ K (131C). For the expected fluid pressure in the rock matrix and hydraulic fracture, the assumed fluid temperatures are out of phase change ranges. The initial content of the gas phase was taken as 40%. Since the temperature of the solid and fluid is in the range from 277.15 K (4 °C) to 408.15 K (135 °C), we assumed a constant heat transfer coefficient and specific heat of the solid and fluid. This simplification is reasonable.

Fig. 7 shows the pressure distribution in the specimen after the hydraulic fracture reaches the upper specimen's boundary for different initial temperatures of the rock matrix. The duration of the fracture propagation for each simulation was similar and ranged
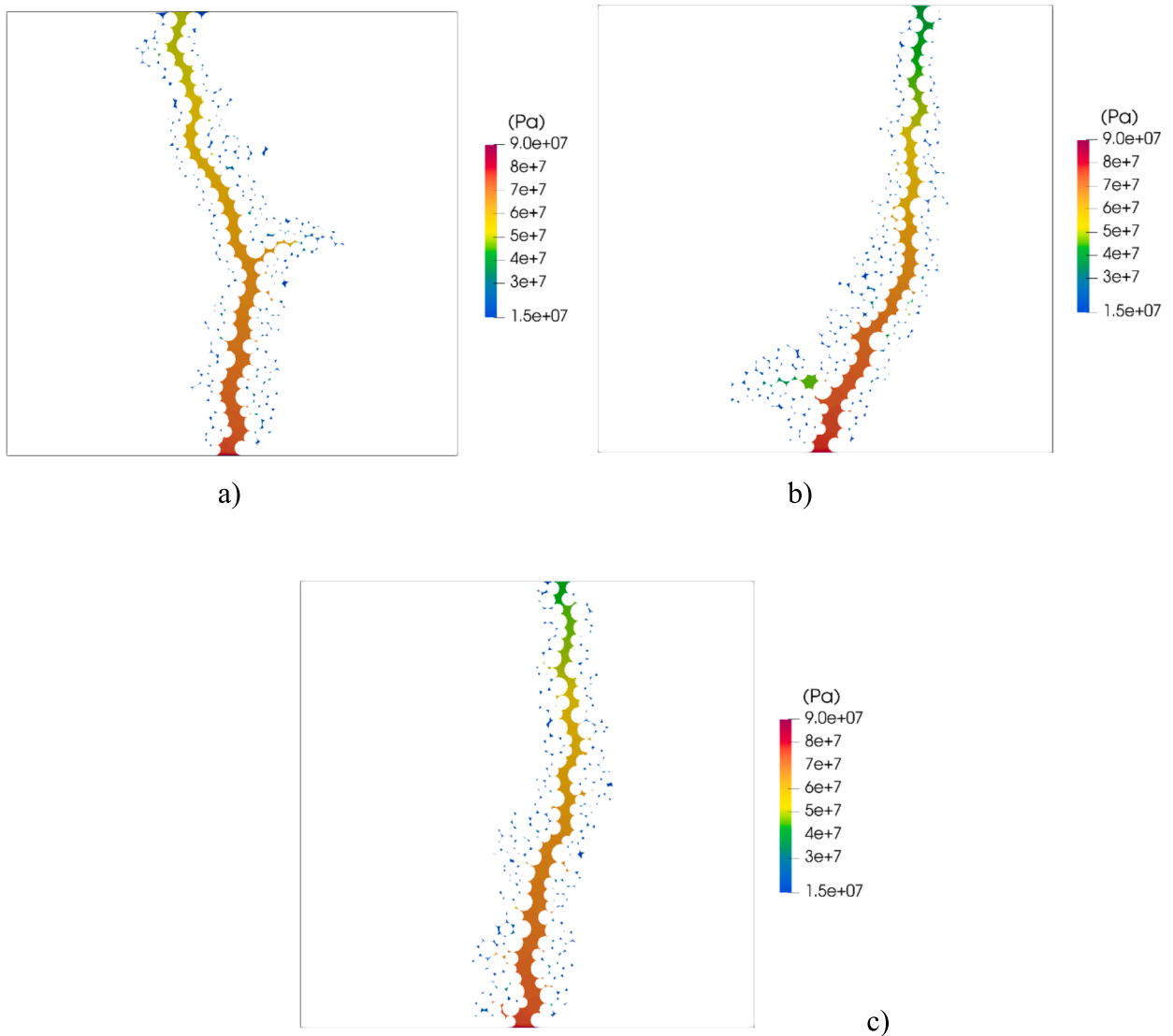
Fig.7. Pressure distribution in rock specimen for different initial temperatures of rock matrix: a) $Trm = 338.15$ K (after 18.2 ms), b) $Trm = 368.15$ K (after 20.3 ms) and c) $Trm = 408.15$ K (after $t = 19.1$ ms).

from $t = 18.2$ ms to $t = 20.3$ ms. The pressure distribution in the fracture was very similar for all rock matrix temperatures (Fig. 8). However, the fluid pressure at the top of the fracture dropped from 5.03 MPa to 4.09 MPa as the temperature of the rock matrix increased from 338.15 K (65 °C) to 408.15 K (135 °C). The fracture shape differed in each simulation (Fig. 7), caused by the different fluid density resulting from the various fluid temperature. However, the relative length of the hydraulic fracture l_{rel} (defined as the ratio of the length of the fracture to the height of the specimen) was the same and equal to $l_{rel} = 1.1$.

The fluid phase density was in the range 979.7 kg/m^3 and 1036.3 kg/m^3 for $Trm = 338.15$ K, 952.0 kg/m^3 and 1036.3 kg/m^3 $Trm = 368.15$ K, and 910.3 kg/m^3 and 1036.3 kg/m^3 for $Trm = 408.15$ K. The gas phase density was in the range 152.4 kg/m^3 and 694.1 kg/m^3 for $Trm = 338.15$ K and 138.3 kg/m^3 and 694.1 kg/m^3 for $Trm = 368.15$ K, and 23.6 kg/m^3 and 694.1 kg/m^3 for $Trm = 408.15$ K. The highest density of both phases was the same for each simulation, while the lowest density of both phases decreased with increasing rock matrix temperature.

The temperature distribution in the specimen for different initial temperatures of the rock matrix Trm is shown in Fig. 8. The fluid temperature difference between the bottom and the top of the specimen's fracture strongly increased with the initial temperature of the rock matrix Trm. The maximum fluid temperature difference was $\Delta T_f = 50.13$ K for $Trm = 338.15$ K, $\Delta T_f = 76.28$ K for $Trm = 368.15$ K, and $\Delta T_f = 110.47$ K for $Trm = 408.15$ K.

After the hydraulic fracture reached the specimen top, the temperature difference between the rock matrix and the fluid in the fracture near the injection point was still very high (Fig. 8). The fluid temperature changed from $\Delta T_f = 56.8$ K (case 'a') to $\Delta T_f = 106.1$ K (case 'c'). At the same time, the temperature difference between the injected fluid and the rock matrix was only slightly higher and
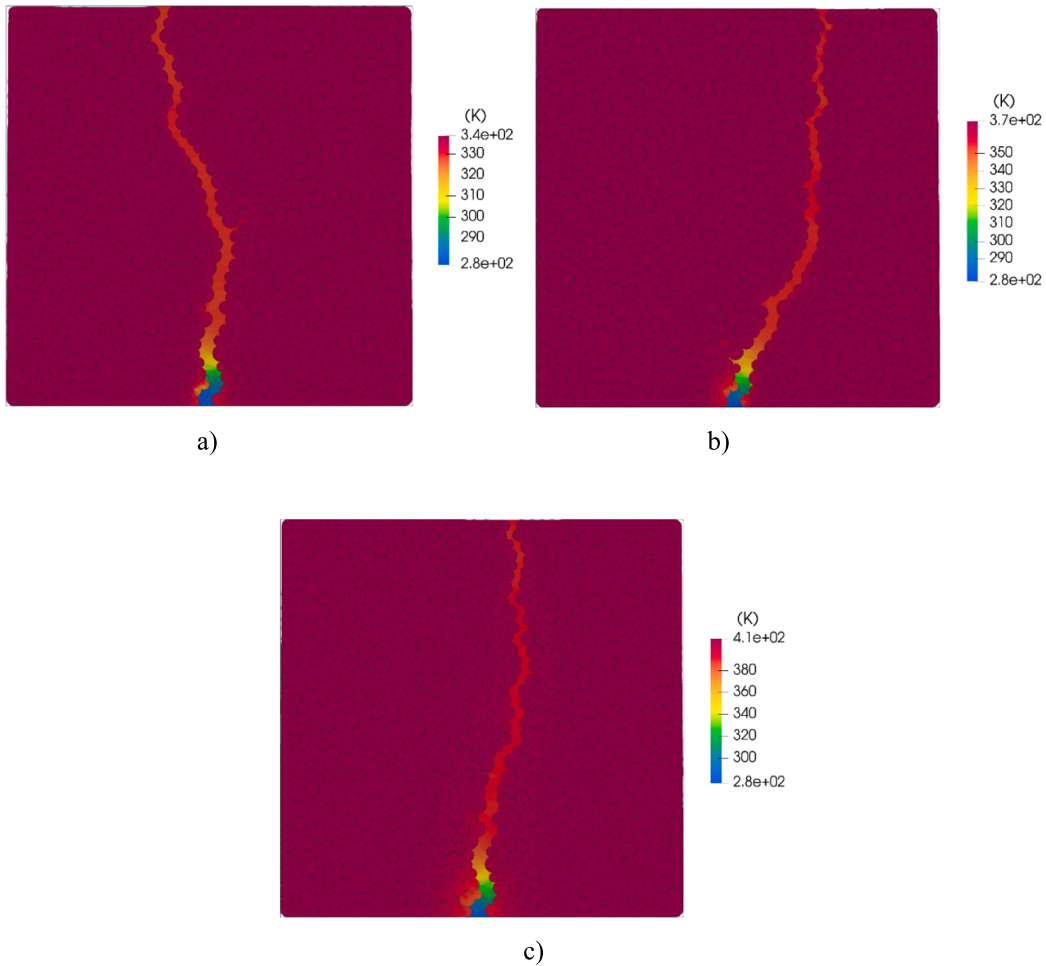
Fig.8. Temperature distribution in rock specimen for different initial temperatures of rock matrix: a) $Trm = 338.15$ K (after $t = 18.2$ ms), b) $Trm = 368.15$ K (after $t = 20.9$ ms) and c) $Trm = 408.15$ K (after $t = 19.1$ ms).

amounted to $\Delta T = 61$ K (case 'a'), $\Delta T = 91$ K (case 'b'), and $\Delta T = 131$ K (case 'c'). It can be observed that the fluid heated up very quickly near the injection point, while the temperature of the fluid away increased only slightly from the injection point.

During the hydraulic fracturing process, the heat was transferred from the warm rock matrix to the cold fluid (Fig. 9). After the hydraulic fracture reached the specimen top, the maximum temperature drop of the rock matrix surrounding the fracture was $\Delta Trm = 17.7$ K (case 'a'), $\Delta Trm = 20.2$ K (case 'b') and $\Delta Trm = 25.8$ K (case 'c'). It should be noted that the simulations mimicked the hydraulic fracturing process in a very small specimen and were stopped when the hydraulic fracture reached the specimen top ($t \cong 20$ ms). In a real hydraulic fracturing process, the process takes much longer. As a consequence, the temperature's drop of the rock matrix would be much greater, resulting in high-temperature stresses in the rock matrix which might contribute to additional cracks due to thermal strains (leading to an increase in the rock permeability). This process will be numerically studied in-depth shortly.

After initiating a hydraulic fracture, advection strongly dominated the energy transport in the fluid (Fig. 10). The maximum advection in the fluid, expressed as the amount of energy [J] per unit of time [s], was almost 10 times higher than the maximum diffusion and was equal to 1100 W. The maximum advection occurred at the first bend of the fracture just after passing its first straight section, i.e. after approaching the first obstacle for the flowing fluid.

5.2. Effect of fluid dynamic viscosity

The dynamic viscosity of liquids decreases and of gases increases with increasing temperature. The influence of the dynamic viscosity of the injected fluid on the initiation and propagation of a single hydraulic fracture under non-isothermal conditions was again investigated for the initial gas content of 40%. The temperature of the injected fluid was constant and was equal to $T_f = 277.15$ K (4 °C) with the initial temperature of the rock matrix $Trm = 408.16$ K (135 °C). Two different dynamic viscosities of the injected liquid were compared: 4.06×10^{-4} Pa·s (case 'a', Table 1) and 2.44×10^{-4} Pa·s (case 'b').

The temperature distribution in the specimen after the hydraulic fracture reached the upper boundary for different dynamic
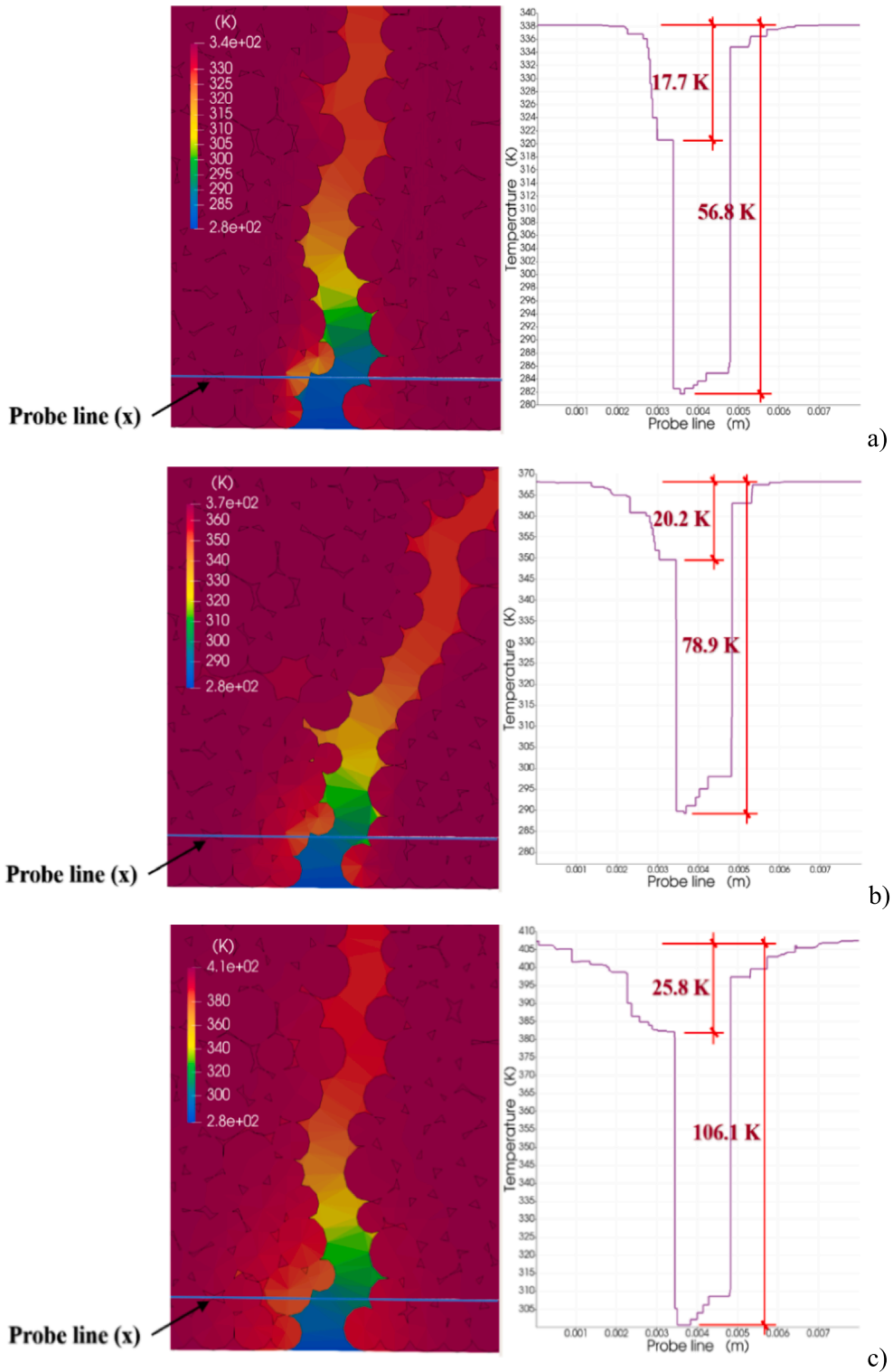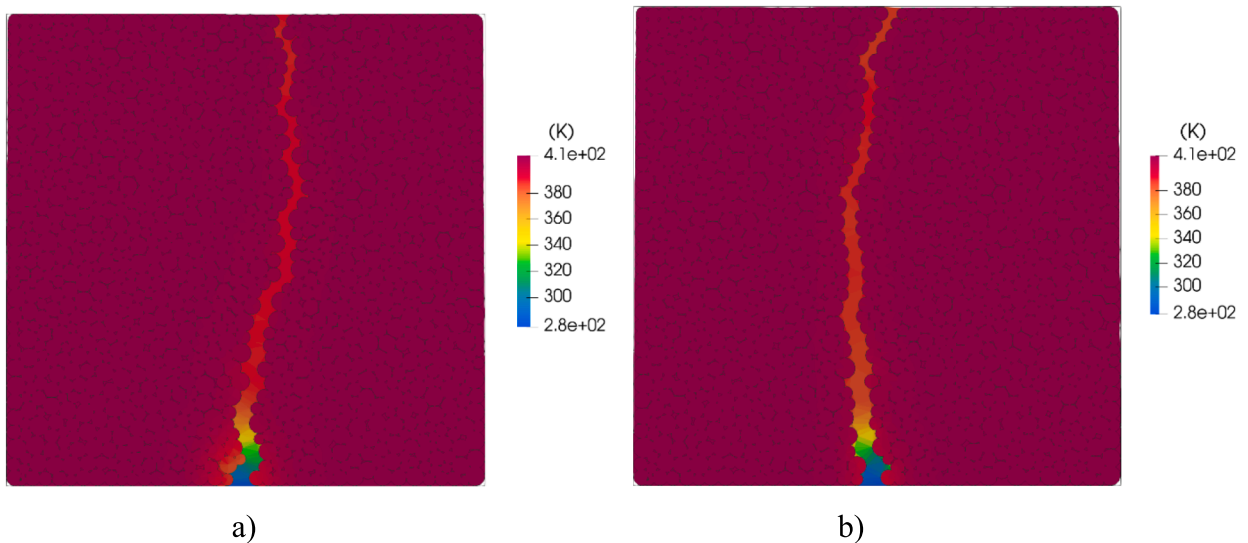
Fig.9. Temperature distribution in specimen close to injection point and along the probe line for different initial temperatures of rock matrix: a) $Trm = 338.15$ K (after $t = 18.2$ ms), b) $Trm = 368.15$ K (after $t = 20.9$ ms) and c) $Trm = 408.15$ K (after $t = 19.1$ ms).
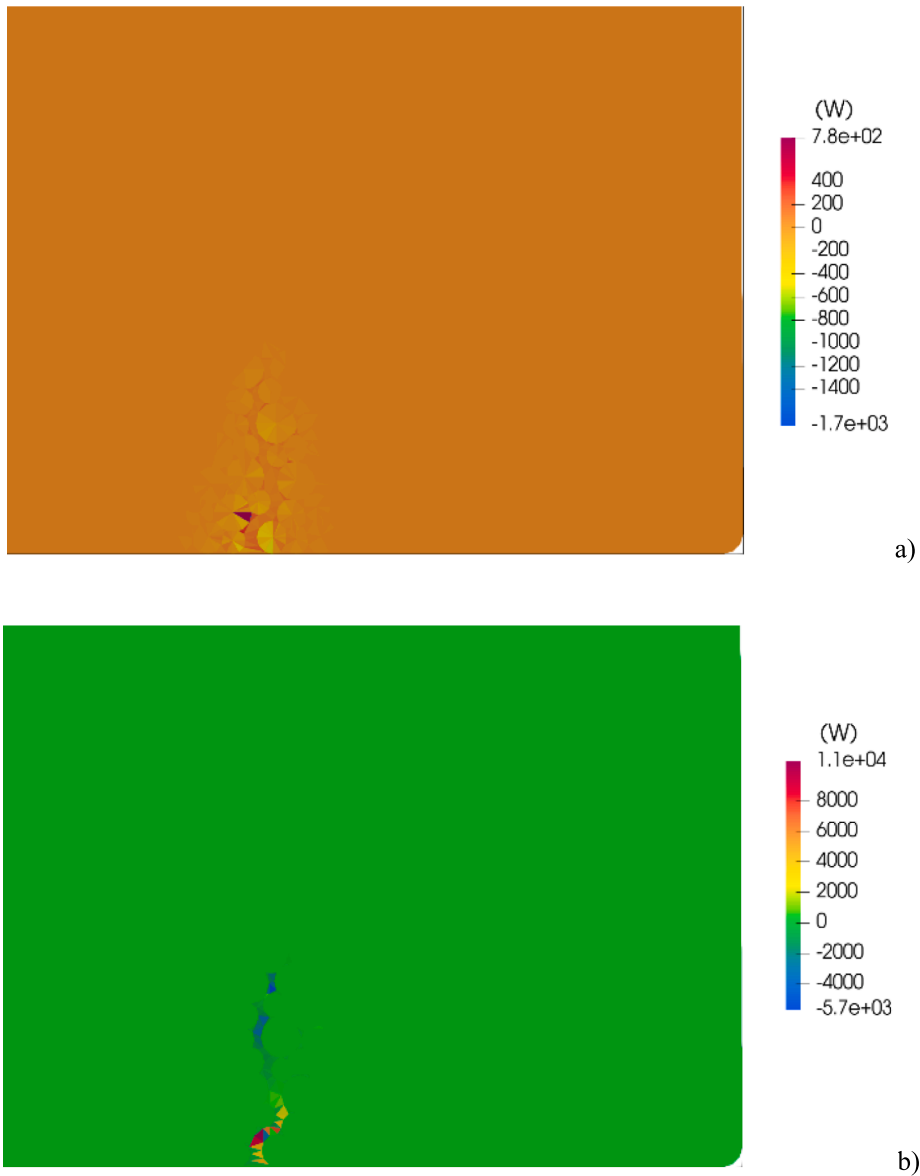
Fig.10. Energy transported by diffusion (a) and advection (b) in terms of energy amount [J] per time unit [s]) in rock matrix specimen for its initial temperature of $Trm = 408.15$ K after $t = 2.5$ ms of initial stage of hydraulic fracture propagation.

viscosities of the fluid phase is illustrated in Fig. 11. The duration of the fracture propagation process was very different in both cases. For the high dynamic viscosity of the fluid (case 'a'), the hydraulic fracturing process lasted nearly twice longer ($t = 19.1$ ms) than for the low dynamic viscosity ($t = 11.1$ ms, case 'b'). The hydraulic fracture was more curved for the high dynamic viscosity of the fluid. Thus, when the dynamic viscosity was lower, the propagation process was shorter and the fluid exchanged less heat with the surrounding solid. The relative length of the hydraulic fracture $l_{ref} = 1.09$ was greater by 5% for fluid with high dynamic viscosity (Fig. 11a) than for fluid with low dynamic viscosity $l_{ref} = 1.05$ (Fig. 11b).

The maximum temperature difference above the injection point between the fluid and the rock matrix was $\Delta T = 25.8$ K (case 'a') and was higher by 10 K than in case 'b' ($\Delta T = 15.5$ K) (Fig. 12). However, the drop in the fluid temperature at the injection point was lower by 10 K for the high fluid dynamic viscosity ($T_f = 106.1$ K) as compared to the low fluid dynamic viscosity ($T_f = 116.6$ K). This difference may be explained by the higher fluid velocity and related advection in flowing fluid for the lower dynamic viscosity. Taking into account the results of the simulations, it can be concluded that the dynamic viscosity of the injected fluid has a significant impact on the course of the hydraulic fracturing process in non-isothermal conditions as it was reported in laboratory experiments [12].

Fig. 11. Temperature distribution in the specimen for different dynamic viscosities of injected fluid: a) $\mu_q = 4.06 \times 10^{-4}$ Pa·s (after $t = 19.1$ ms) and $\mu_q = 2.44 \times 10^{-4}$ Pa·s (after $t = 11.1$ ms).

5.3. Effect of gas phase content

The influence of the initial content of the gas phase on the process of initiation and propagation of the hydraulic fracture was already investigated by the authors, however in isothermal conditions [17]. The initial content of the gas phase had a great influence on the fracture propagation speed and its shape. However, in real conditions, the heat transfer in the fluid and the rock matrix is a factor that can strongly affect the hydraulic fracture propagation process. Due to the significantly different thermal properties of fluid phases, it is expected that the effect of heat transfer on the hydraulic fracture propagation process is strongly dependent on the initial content of the gas phase in the rock matrix. Therefore, the influence of the initial content of the gas phase on the process of initiation and propagation of the hydraulic fracture under non-isothermal conditions was investigated for several different initial contents of the gas phase in the rock matrix: 0%, 20%, 40%, and 60%. The obtained results were compared with the simulation results of the hydraulic fracturing process in isothermal conditions and for the initial content of the gas phase of 0%, typical conditions found in most existing coupled DEM-CFD models. The initial temperature of the rock matrix was $Trm = 343.15$ K, and the temperature of the injected fluid was again $T_f = 277.15$ K in all simulations carried out in non-isothermal conditions.

Fig. 13 shows the pressure distribution in the rock specimen after the hydraulic fracture reached the specimen's upper boundary for different initial contents of the gas phase in the rock matrix.

The greater the initial content of the gas phase in the rock matrix, the significantly slower the hydraulic fracture propagation velocity. The difference in fracture propagation time between the initial 0% ($t = 1.3$ ms) and 60% ($t = 24.8$ ms) gas phase content was huge (about 20 times). Fractures also differed in shape. When the initial gas content was 0%, the hydraulic fracture was almost straight and vertical (Fig. 13a). When the initial gas content was greater than zero (Fig. 13b-13d), the shape of the hydraulic fracture was more curved, leading to an increase in its overall length.

The result of heat transfer in the fluid and the rock matrix is shown in Fig. 14. The greater the initial content of the gas phase in the rock matrix, the greater the drop in fluid temperature in the hydraulic fracture (Fig. 14). This is because the duration of the process was longer When the initial content of the gas phase was high (Fig. 14d), the duration of the hydraulic fracturing process took a very long time. In the absence of a gas phase in the rock matrix (Fig. 14a), the drop in fluid temperature was limited to the area close to the injection point. This was because the water is an almost incompressible fluid and a very small amount of injected water was needed to build up pressure and initiate damage. As a consequence, a very small amount of cold water penetrated the rock matrix and then the fracture. The heat was transferred mainly by diffusion and not by advection. In contrast to the absence of the gas phase, a large water amount was required to compress the gas phase and to increase the pressure for the high gas phase content (Fig. 15d). In this case, advection dominated and carried large energy, and diffusion was of marginal importance. This affected the cooling rate of the matrix grains surrounding the fracture (Fig. 15) and the temperature of the fluid in the hydraulic fracture. If the initial content of the gas phase was high enough (Fig. 15), the grains of the rock matrix were significantly cooled near the injection slot and along the fracture. The maximum temperature drop of the rock matrix grains was 8.1 K with the initial content of the gas phase of 60%. It should be noted again, that the hydraulic fracturing process was performed until the fracture reached the specimen's upper boundary. In reality, the process long continues and the temperature of the grains continues to drop. In contrast to the existing coupled DEM-CFD models, the temperature in the grains was not uniform and the grains deformed according to the spatial temperature changes.

During the hydraulic fracturing process, the heat was transferred in the fluid by diffusion and advection, while in solids by conduction (Fig. 16). In the absence of the gas phase in the rock matrix (Fig. 16a), advection in the fracture was intense in the area very

a)

b)
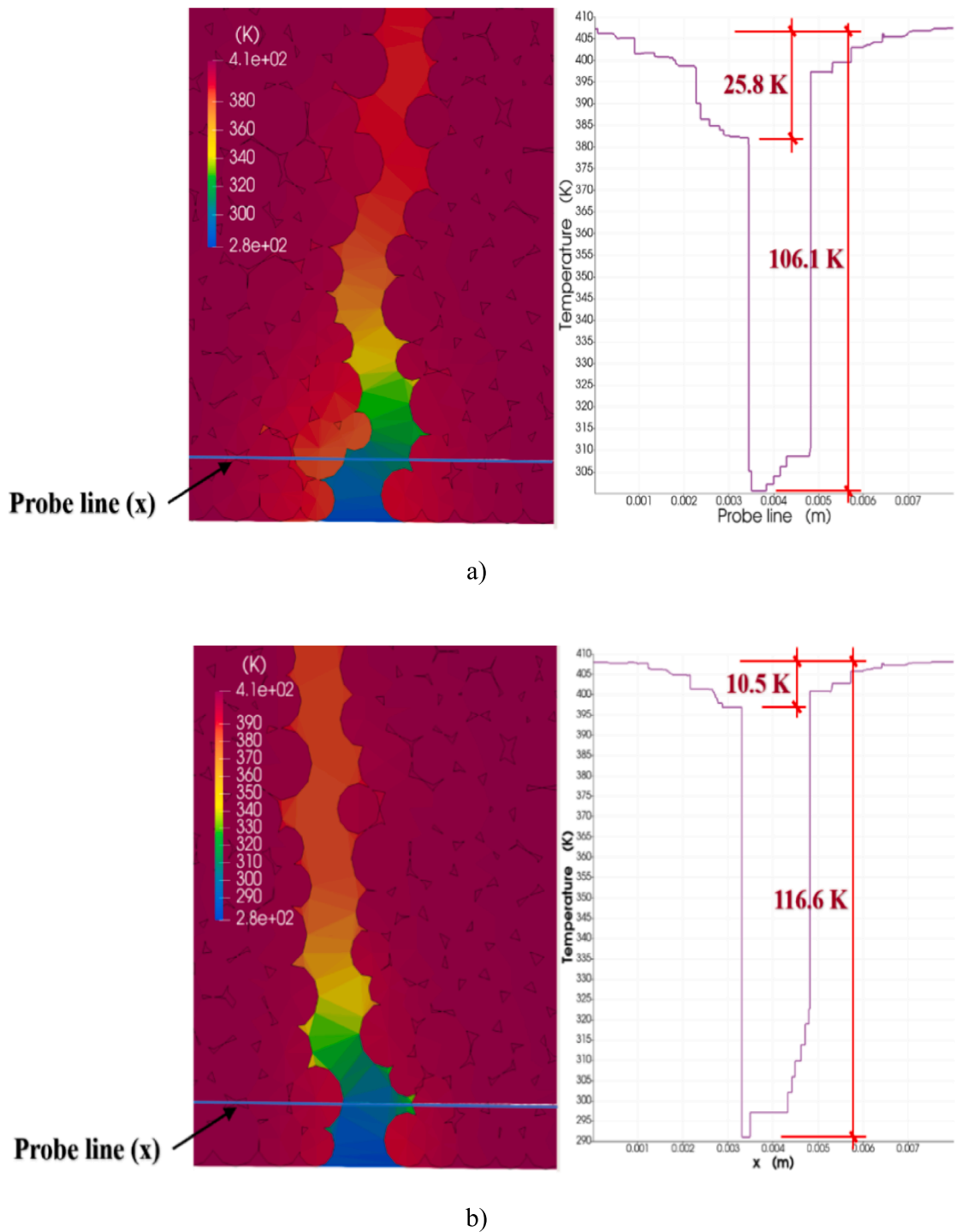
Fig.12. Temperature distribution in specimen close to injection point and along probe line for different fluid dynamic viscosities: a) high viscosity $\mu_q = 4.06 \times 10^{-4}$ Pa·s (after $t = 19.1$ ms) and b) low viscosity $\mu_q = 2.44 \times 10^{-4}$ Pa·s (after $t = 11.1$ ms).

close to the injection slot (2100 W) and in the area close to the upper boundary of the specimen (-510 W). Outside these areas, the fluid advection was small and changed slightly around 0 W. Small diffusion (-62 W) was observed only in the area close to the injection point (Fig. 16b). Outside this area, the fluid diffusion was close to 0.0 W. This resulted in a small fluid temperature drop only in the fracture very close to the injection point (Fig. 16a). In contrast to the absence of the gas phase in the rock matrix, for the initial content of the gas phase of 60%, the heat transfer in the fluid and rock matrix was more intense (Fig. 16). The advection in the fluid in the fracture varied
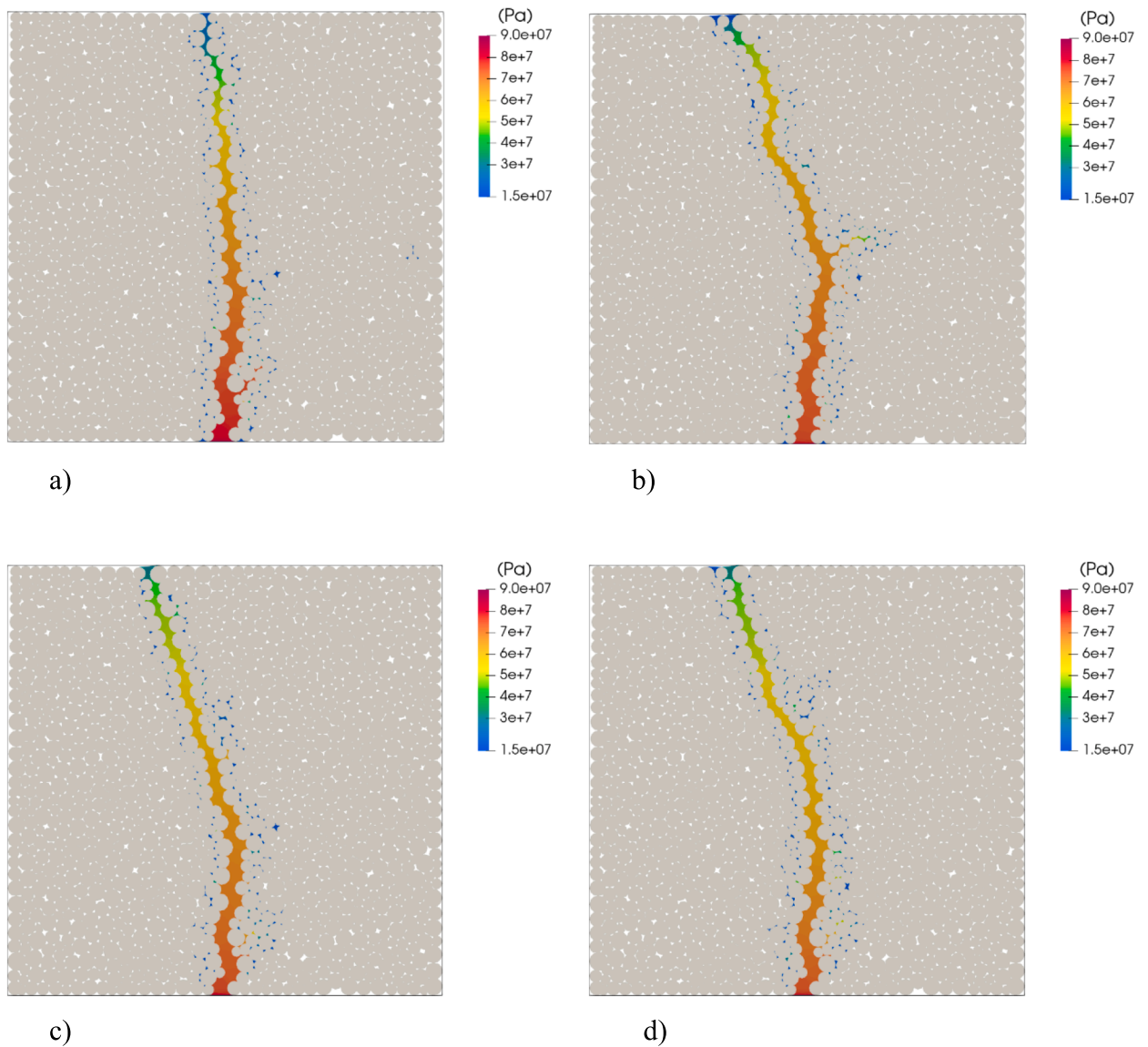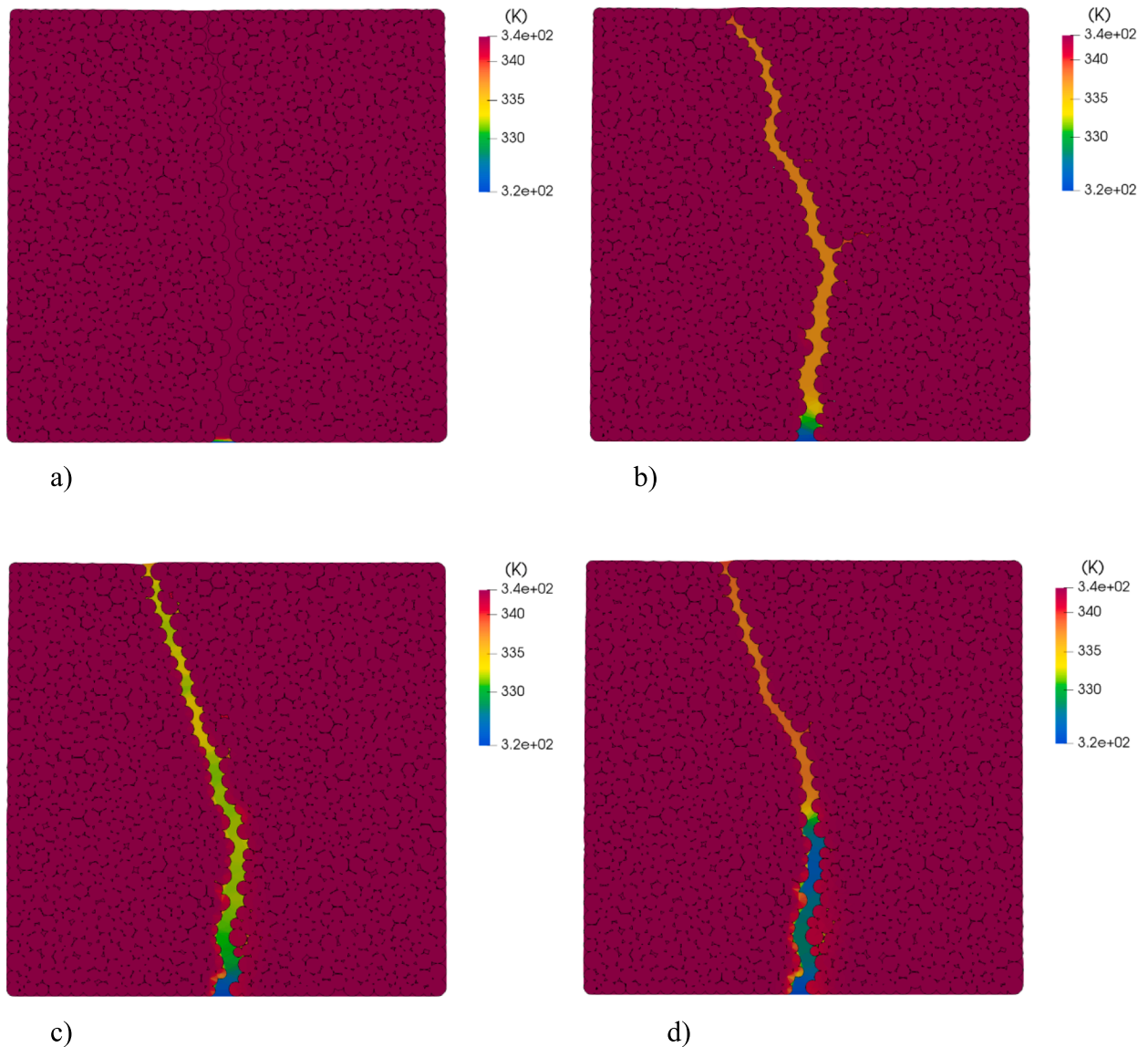
Fig.13. Pressure distribution in rock specimen for different initial contents of gas phase in rock matrix: a) 0% (after $t = 1.3$ ms), b) 20% (after $t = 9.5$ ms), c) 40% (after $t = 17.7$ ms) and d) 60% (after $t = 24.8$ ms).

from about 260 W to about −1200 W along the fracture, reducing and increasing the fluid temperature, respectively (Fig. 16c). Diffusion in the fluid was relatively small and did not exceed 40 W along the entire fracture (Fig. 16d). However, the diffusion in the grains surrounding the fracture was much greater and reached 120 W, lowering their temperature. This means that the heat exchange between the fluid and solid was intense for the high initial gas phase content, and the grains surrounding the fracture were then strongly cooled.

6. Summary and conclusions

The fully coupled DEM/CFD-based thermo-hydro-mechanical approach was used in this work to simulate small-scale hydraulic fracturing in cohesive granular specimens with low porosity imitating rock under non-isothermal conditions. The approach accurately discretized the geometry of pores in the rock mass and considered the two-phase laminar flow of the fracturing fluid in the flow network built of channels and heat transfer in fluid and solid. The approach showed its capability to capture the development of hydraulic fractures in rocks and fracturing fluid (liquid/gas) pressures and temperatures. The effects of the temperature difference between the rock matrix and the injected fluid, the dynamic viscosity of the injected fluid, and the gas content in the rock matrix were numerically studied, which proved to be pronounced, showing growth with increasing hydraulic fracturing time. The following conclusions may be offered from our 2D mesoscopic simulations for small rock segments with one injection slot:

22

Fig.14. Temperature distribution in rock specimen for different initial contents of gas phase in rock matrix: a) 0% (after $t = 1.3$ ms), b) 20% (after $t = 9.5$ ms), c) 40% (after $t = 17.7$ ms) and d) 60% (after $t = 24.8$ ms).

- The impact of the temperature difference between the rock matrix and the injected fluid on the hydraulic fracture shape was visible. The fluid temperature difference between the bottom and the top of the fracture strongly increased with the initial temperature of the rock matrix. The lowest density of both phases decreased with increasing rock matrix temperature. Advection strongly dominated the energy transport in the fluid; it was significantly higher than the diffusion energy.
- For the low dynamic viscosities of the injected fluid, the hydraulic fracturing process lasted shorter and the hydraulic fracture shape was, thus, more vertical. The maximum temperature difference between the fluid and the rock matrix was higher for the high dynamic viscosity above the injection point and lower at the injection point.
- The greater the initial content of the gas phase in the rock matrix, the more curved the hydraulic fracture, the significantly slower the hydraulic fracture propagation velocity, and the greater the fluid temperature reduction in the hydraulic fracture. The heat exchange between the fluid and solid was more intense for the high initial gas content, and the grains surrounding the fracture were then strongly cooled.
- The development of thermal cracks may contribute to a noticeable increase in crack branching, leading to rock permeability growth.
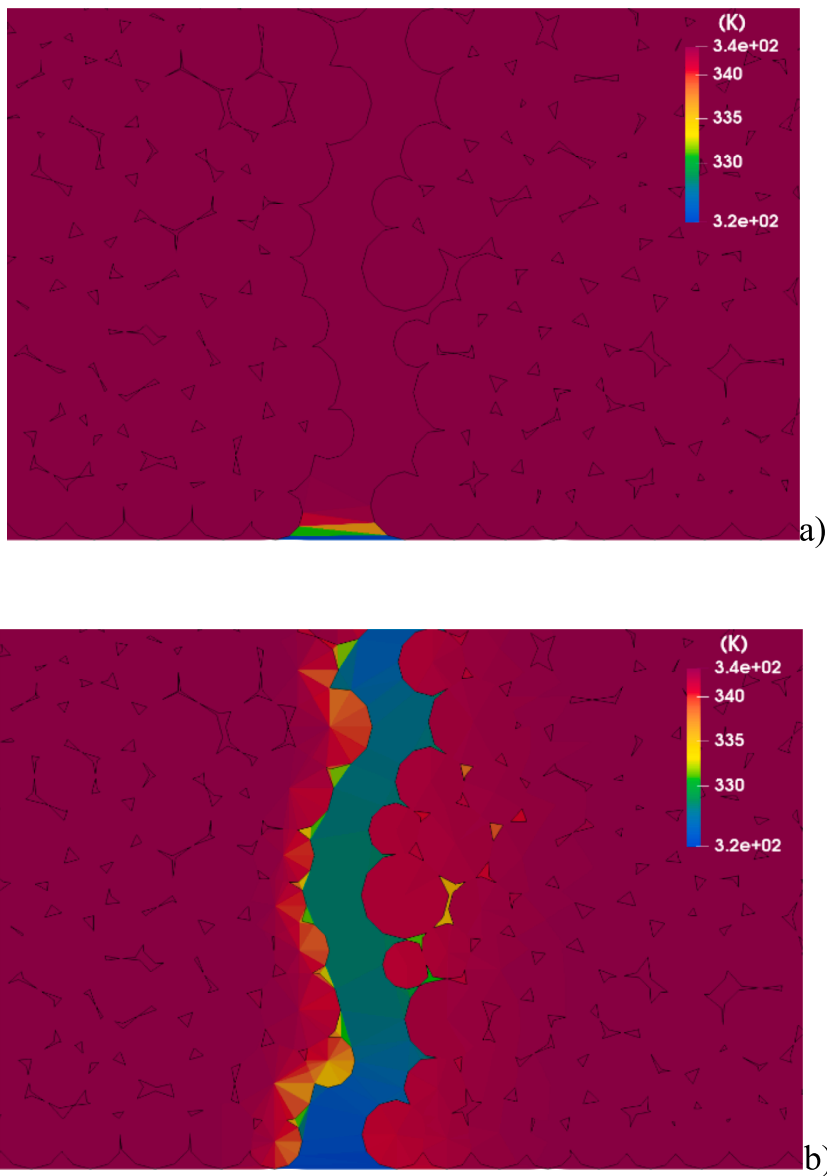
Fig.15. Temperature distribution in rock specimen close to injection point for different initial contents of gas phase in rock matrix: a) 0% (after $t = 1.3$ ms) and b) 60% (after $t = 24.8$ ms).

CRediT authorship contribution statement

M. Krzaczek: Writing – original draft, Visualization, Validation, Software, Methodology, Investigation, Formal analysis, Conceptualization. **J. Tejchman:** Writing – review & editing, Supervision, Project administration, Funding acquisition, Conceptualization.
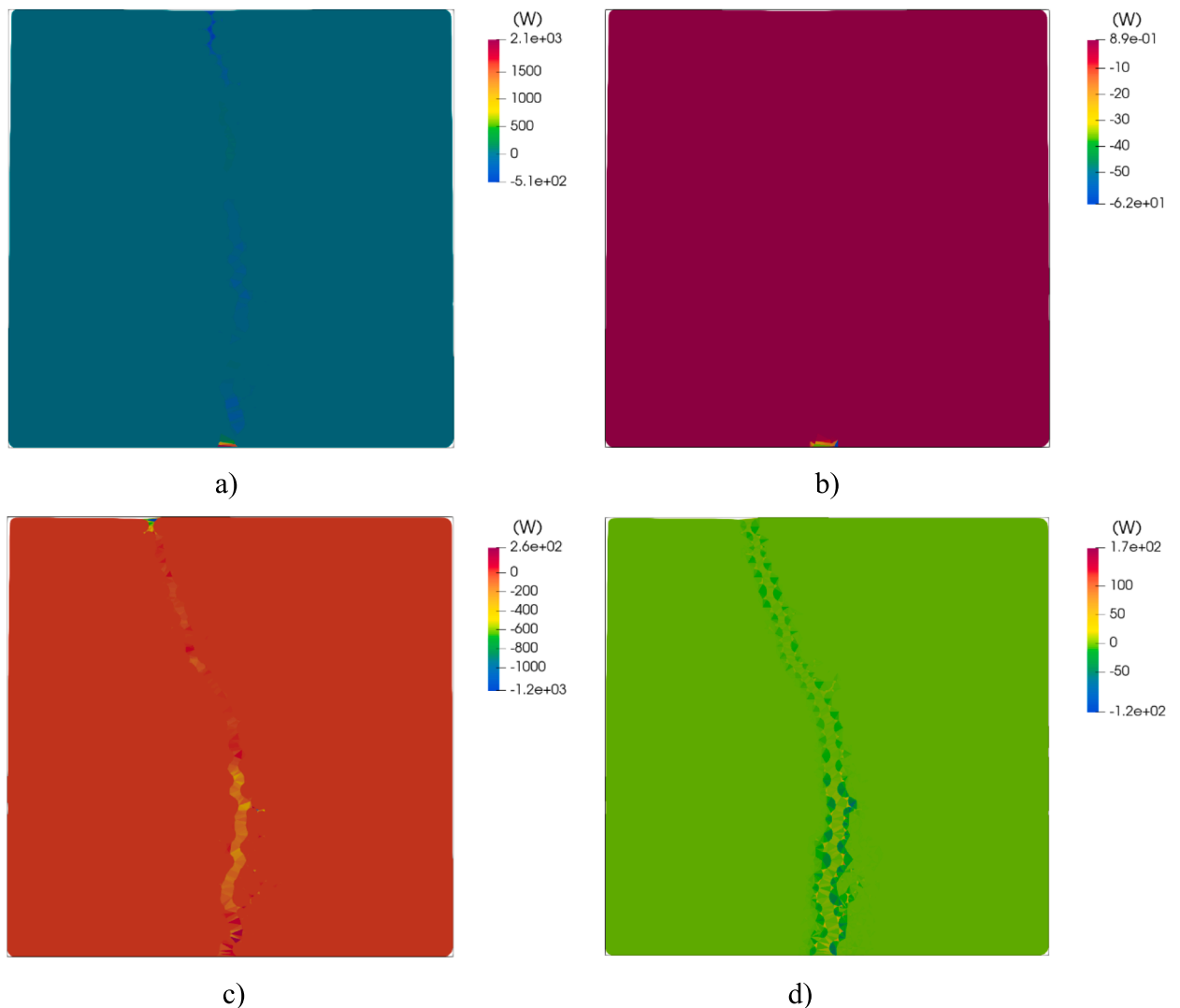
Declaration of Competing Interest

The authors declare that they have no known competing financial interests or personal relationships that could have appeared to influence the work reported in this paper.

Data availability

Data will be made available on request.

Fig.16. Energy transported by diffusion and advection in rock specimen for different initial contents of gas phase in rock matrix (in terms of energy amount [J] per time unit [s]): a) advection for initial gas phase of 0%, b) diffusion for initial gas phase of 0%, c) advection for initial gas phase of 60% and d) diffusion for initial gas phase of 60%.

Acknowledgements

References

[1] Rijken P, Cooke ML. Role of shale thickness on vertical connectivity of fractures: application of crack-bridging theory to the Austin Chalk. Tectonophysics 2001; 337:117–33.
[2] Gale JFW, Reed RM. Natural fractures in the Barnett Shale and their importance for fracture treatments. AAPG Bull 2007;91(4):603–22.
[3] Beckwith R, Hydraulic R. Fracturing: the fuss, the facts, the future. J Pet Technol 2010;62(12):34–41.
[4] Deo M, Sorkhabi R, McLennan J, Bhide R, Zhao N, Sonntag R. Evans, J. Gas production forecasting from tight gas reservoirs: Integrating natural fracture networks and hydraulic fractures. Final Report to RPSEA; 2013. p. 07122–44.
[5] Haifeng Z, Hang J, Guohua C, Yawei L, Jun S, Peng R. New insight into mechanisms of fracture network generation in shale gas reservoir. J Pet Sci Eng 2013; 110:193–8.
[6] Gandossi L, von Estorff U. An overview of hydraulic fracturing and other formation stimulation technologies for shale gas production. *Scientific and Technical Research Reports*. Joint Research Centre *of the* European Commission Publications Office of the European Union 2015. https://doi.org/10.2790/379646.
[7] Norris JQ, Turcotte DL, Moores EM, Brodsky EE, Rundle JB. Fracking in tight shales: what is it, what does it accomplish, and what are its consequences? Annu Rev Earth Planet Sci 2016;44(1):321–51.

[8] Bazant ZP, Salviato M, Chau VT, Viswanathan H, Zubelewicz A. Why fracking works. J Appl Mech 2014;81(10):4028192.

[9] Chau VT, Li C, Rahimi-Aghdam S, Bazant ZP. The enigma of large-scale permeability of gas shale: pre-existing or frac-induced? J Appl Mech 2017;84:061008.

[10] Chau VT, Bazant ZP, Su Y. Growth model for large branched three-dimensional hydraulic crack system in gas or oil shale. Phil Trans R Soc 2016;374:20150418.

[11] Rahimi-Aghdam S, Chau V-T, Lee H, Nguyen H, Li W, Karra S, et al. Branching of hydraulic cracks enabling permeability of gas or oil shale with closed natural fractures. Proc Natl Acad Sci USA 2019;116(5):1532–7.

[12] Li W.F., Frash L.P., Carey J.W., Welch H.J., Meng M., Nguyen H., Viswanathan H., Rougier E., Lei Z., Rahimi-Aghdam S., Bazant Z.P.. Injection Parameters that Promote Branching of Hydraulic Cracks. *Geophys. Res. Lett.*, 2021; 48 (12) e2021GL093321.

[13] Li W, Frash LP, Lei Z, Carey JW, Chau VT, Rougier E, et al. Investigating poromechanical causes for hydraulic fracture complexity using a 3D coupled hydro-mechanical model. J Mech Phys Solids 2022;169:105062.

[14] Mróz Z, Zacharski A. Cool layer deformation of rock-gas outburst and initiation. In: Litwiniszyn J, editor. Strata as Multi-Phase Medium. AGH Publisher; 1990. p. 537–71. in Polish.

[15] Krzaczek M, Nitka M, Tejchman J. A novel DEM-based pore-scale thermal-hydro-mechanical model for fractured non-saturated porous materials. Acta Geotech 2023;18:2487–512.

[16] Krzaczek M, Nitka M, Kozicki J, Tejchman J. Simulations of hydro-fracking in rock mass at meso-scale using fully coupled DEM/CFD approach. Acta Geotech 2020;15(2):297–324.

[17] Krzaczek M, Nitka M, Tejchman J. Effect of gas content in macropores on hydraulic fracturing in rocks using a fully coupled DEM/CFD approach. Int J Numer Anal Meth Geomech 2021;45(2):234–64.

[18] Abdi A, Krzaczek M, Tejchman J. Comparative study of high-pressure fluid flow in densely packed granules using a 3D CFD model in a continuous medium and a simplified 2D DEM-CFD approach. Granul Matter 2022;24(1):1–25.

[19] Abdi R, Krzaczek M, Tejchman J. Simulations of high-pressure fluid flow in a pre-cracked rock specimen composed of densely packed bonded spheres using a 3D CFD model and simplified 2D coupled CFD-DEM approach. Powder Technol 2023;417:118238.

[20] Krzaczek M, Nitka M, Tejchman J. Modelling hydraulic and capillary-driven two-phase fluid flow in unsaturated concretes at the meso-scale with a unique coupled DEM-CFD technique. Int J Numer Anal Methods Geomech 2023;47(1):23–53.

[21] Olivella S, Gens A, Carrera J, Alonso E. Numerical formulation for a simulator (code bright) for the coupled analysis of saline media. Eng Comput 1996;13(7): 87–112.

[22] Kolditz O, Bauer S, Bilke L, Böttcher N, Delfs JO, Fischer T, et al. Opengeosys: an open-source initiative for numerical simulation of thermo-hydro-mechanical/ chemical (thm/c) processes in porous media. Environ Earth Sci 2012;67(2):589–99.

[23] Zareidarmiyan A, Salarirad H, Vilarrasa V, Kim K-I, Lee J, Min K-B. Comparison of numerical codes for coupled thermo-hydro-mechanical simulations of fractured media. J Rock Mech Geotech Eng 2020;12(4):850–65.

[24] Rühaak W., Sass I. Applied thermo-hydro-mechanical coupled modeling of geothermal prospection in the Northern Upper Rhine Graben. Proceedings of Thirty-Eighth Workshop on Geothermal Reservoir Engineering, Stanford University, Stanford, California, 2013.

[25] Selvadurai APS, Suvorov AP, Selvadurai PA. Thermo-hydro-mechanical processes in fractured rock formations during a glacial advance. Geosci Model Dev 2015; 8:2167–85.

[26] Li T, Tang C, Rutqvist J, Hu M. TOUGH-RFPA: Coupled thermal-hydraulic-mechanical rock failure process analysis with application to deep geothermal wells. International Journal of Rock Mechanics & Mining Sciences 2021;142:104726.

[27] Rutqvist J, Wu Y-S, Tsang C-F. A modeling approach for analysis of coupled multiphase fluid flow, heat transfer, and deformation in fractured porous rock. Int J Rock Mech Min Sci 2022;39(4):429–42.

[28] Yan C, Zheng H. A coupled thermo-mechanical model based on the combined finite-discrete element method for simulating thermal cracking of rock. Int J Rock Mech Min Sci 2017;91:170–8.

[29] Yan C, Xie X, Ren Y, Ke W, Wang G. A FDEM-based 2D coupled thermo-hydro-mechanical model for multiphysical simulation of rock fracturing. I J of Rock Mechanics & Mining Sciences 2022;149:104964.

[30] Deen NG, Kriebitzsch SH, van der Hoef MA, Kuipers J. Direct numerical simulation of flow and heat transfer in dense fluid–particle systems. Chem Eng Sci 2012; 81:329–44.

[31] Chen Z, Jin X, Wang M. A new thermo-mechanical coupled DEM model with non-spherical grains for thermally induced damage of rocks. J Mech Phys Solids 2018;116:54–69.

[32] Tomac I, Gutierrez M. Coupled hydro-thermo-mechanical modeling of hydraulic fracturing in quasi-brittle rocks using BPM-DEM. Journal Rock Mech Geotech Eng 2017;9(1):92–104.

[33] Caulk R, Sholtès L, Krzaczek M, Chareyre B. A pore-scale thermo–hydro-mechanical model for particulate systems. Comput Methods Appl Mech Engrg 2020;372: 113292.

[34] Jiao K, Han D, Li J, Bai B, Gong L, Yu Bo. A novel LBM-DEM based pore-scale thermal-hydro-mechanical model for the fracture propagation process. Comput Geotech 2021;139:104418.

[35] Yang B, Chen S, Liu K. Direct numerical simulations of particle sedimentation with heat transfer using the lattice boltzmann method. Int J Heat Mass Transfer 2017;104:419–37.

[36] Nikolić M, Karavelić E, Ibrahimbegovic A, Mišcević P. Lattice element models and their peculiarities. Arch Computat Methods Eng 2018;25(3):753–84.

[37] Cundall P. Fluid formulation for PFC2D. Itasca Consulting Group: Minneapolis, Minnesota; 2000.

[38] Hazzard JF, Young RP, Oates JS. Numerical modeling of seismicity induced by fluid injection in a fractured reservoir 2002;7–10:1023–30.

[39] Al-Busaidi A, Hazzard JF, Young RP. Distinct element modeling of hydraulically fractured Lac du Bonnet granite. J Geophys Res 2005;110:B06302. https://doi. org/10.1029/2004JB003297.

[40] Catalano E, Chareyre B, Barthélémy E. Pore-scale modeling of fluid-particles interaction and emerging poromechanical effects. Int J Numer Anal Meth Geomech 2014;38(1):51–71.

[41] Papachristos E, Scholtès L, Donzé FV, Chareyre B. Intensity and volumetric characterizations of hydraulically driven fractures by hydro-mechanical simulations. Int J Rock Mech Min Sci 2017;93:163–78.

[42] Chareyre B, Cortis A, Catalano E, Barthélemy F. Pore-scale modeling of viscous flow and induced forces in dense sphere packings. Transp Porous Media 2012;94 (2):595–615.

[43] Scholtès L, Chareyre B, Michallet H, Catalano E, Marzougui D. Modeling wave-induced pore pressure and effective stress in a granular seabed. Contin Mech Thermodyn 2015;27(1):305–23.

[44] Che H, O'Sullivan C, Sufian A, Smith ER. A novel CFD-DEM coarse-graining method based on the Voronoi tessellation. Powder Technol 2021;384:479–93.

[45] Yoon JS, Zang A, Stephansson O. Numerical investigation on optimized stimulation of intact and naturally fractured deep geothermal reservoirs using hydro-mechanical coupled discrete particles joints model. Geothermic 2014;52:165–84.

[46] Shimizu H, Murata S, Ishida T. The distinct element analysis for hydraulic fracturing in hard rock considering fluid viscosity and particle size distribution. Int J Rock Mech Mining Sci 2011;48(5):712–27.

[47] Ma X, Zhou T, Zou Y. Experimental and numerical study of hydraulic fracture geometry in shale formations with complex geologic conditions. J Struct Geol 2017;98:53–66.

[48] Liu G, Sun W, Lowinger SM, Zhang Z, Huang M, Peng J. Coupled flow network and discrete element modeling of injected-induced crack propagation and coalescence in brittle rock. Acta Geotech 2019;14(3):843–69.

[49] Zhang G, Li M, Gutierrez M. Numerical simulation of proppant distribution in hydraulic fractures in horizontal wells. J Nat Gas Sci Eng 2017;48:157–68.

[50] Xiao-Dong N, Zhu C, Wang Y. Hydro-mechanical analysis of hydraulic fracturing based on an improved DEM-CFD coupling model at micro-level. J Comput Theor Nanosci 2015;12(9):2691–700.

[51] Zeng J, Li H, Zhang D. Numerical simulation of proppant transport in hydraulic fracture with the upscaling CFD-DEM method. J Nat Gas Sci Eng 2016;33: 264–77.
[52] Zhang G, Sun S, Chao K, Niu R, Liu B, Li Y, et al. Investigation of the nucleation, propagation and coalescence of hydraulic fractures in glutenite reservoirs using a coupled fluid flow-DEM approach. Powder Technol 2019;354:301–13.
[53] Lathama JP, Munjiz A, Mindel J, et al. Modelling of massive particulates for breakwater engineering using coupled FEM/DEM and CFD. Particuology 2008;6: 572–83.
[54] Kozicki J, Donze FV. A new open-source software developer for numerical simulations using discrete modeling methods. Comput Methods Appl Mech Engng 2008;197:4429–43.
[55] Šmilauer V. et al. Yade Documentation 3rd ed. The Yade Project. doi:10.5281/zenodo.5705394 (http://yade-dem.org/doc/), 2021.
[56] Cundall P, Strack O. A discrete numerical model for granular assemblies. Géotechnique 1997;29(1):47–65.
[57] Cundall P, Hart R. Numerical modelling of discontinua. Engng Comput 1992;9:101–13.
[58] Benallal A., Billardon R., Geymonat G. Localization phenomena at the boundaries and interfaces of solids. In Desai C.S. et al (eds.). Proc. of 3rd Int. Conf. Constitutive Laws for Engineering Materials: Theory and Applications, Tucson, Arizona, 1991, pp.387-390.
[59] de Borst R, Sluys LY. Dispersive properties of gradient-dependent and rate-dependent media. Mech Mater 1994;18(2):131–49.
[60] Tejchman J. Shear localization in granular bodies with macro-polar hypoplasticity. Springer Verlag; 2008.
[61] Tomporowski D, Nitka M, Tejchman J. Application of the 3D DEM in the modelling of fractures in pre-flawed marble specimens during uniaxial compression. Engng Fract Mech 2023;277:108978.
[62] Nitka M, Tejchman J. Modelling of concrete behaviour in uniaxial compression and tension with DEM. Granul Matter 2015;17(1):145–64.
[63] Widulinski L, Tejchman J, Kozicki J, Leśniewska D. Discrete simulations of shear zone patterning in sand in earth pressure problems of a retaining wall. Int J Solids Struct 2011;48(7–8):1191–209.
[64] Kozicki J, Niedostatkiewicz M, Tejchman J, Mühlhaus H-B. Discrete modelling results of a direct shear test for granular materials versus FE results. Granular Matter 2013;15(5):607–27.
[65] Kozicki J, Tejchman J, Műhlhaus H-B. Discrete simulations of a triaxial compression test for sand by DEM. Int J Num Anal Meth Geomech 2014;38:1923–52.
[66] Kozicki J, Tejchman J. Relationship between vortex structures and shear localization in 3D granular specimens based on combined DEM and Helmholtz-Hodge decomposition. Granul Matter 2018;20:48.
[67] Skarżyński L, Nitka M, Tejchman J. Modelling of concrete fracture at aggregate level using FEM and DEM based on x-ray μCT images of internal structure. Engng Fract Mech 2015;10(147):13–35.
[68] Nitka M, Tejchman J. A three-dimensional meso scale approach to concrete fracture based on combined DEM with X-ray μCT images. Cem Concr Res 2018;107: 11–29.
[69] Suchorzewski J, Tejchman J, Nitka M. Discrete element method simulations of fracture in concrete under uniaxial compression based on its real internal structure. Int J Damage Mech 2014;27(4):578–607.
[70] Suchorzewski J, Tejchman J, Nitka M. Experimental and numerical investigations of concrete behaviour at meso-level during quasi-static splitting tension. Theor Appl Fract Mech 2018;96:720–39.
[71] Suchorzewski J, Tejchman J, Nitka M, Bobinski J. Meso-scale analyses of size effect in brittle materials using DEM. Granul Matter 2019;21(9):1–19.
[72] Nitka M, Tejchman J. Meso-mechanical modelling of damage in concrete using discrete element method with porous ITZs of defined width around aggregates. Engng Fract Mech 2020;231:107029.
[73] Tejchman J, Bobiński J. Continuous and discontinuous modeling of fracture in concrete using FEM. Berlin-Heidelberg: Springer; 2013.
[74] Marzec I, Tejchman J. Experimental and numerical investigations on RC beams with stirrups scaled along height or length. Engng Struct 2022;252:113621.
[75] Hökmark H., Lönnqvist M., Fälth B. *Technical Report TR-10-23*: THM-issues in repository rock – thermal, mechanical, thermo-mechanical and hydro-mechanical evolution of the rock at the Forsmark and Laxemar sites. SKB–Swedish Nuclear Fuel and Waste Management Co., 210; pp.26-27.
[76] Reynolds O. An experimental investigation of the circumstances which determine whether the motion of water shall be direct or sinuous, and of the law of resistances in parallel channels 1883;174::935–82. Phil. Trans. Roy. Soc.,.
[77] Batchelor GK, editor. An Introduction to Fluid Dynamics. Cambridge University Press; 2000.
[78] Barmak I, Gelfgat A, Vitoshkin H, Ullmann A, Brauner N. Stability of stratified two-phase flows in horizontal channels. AIP Physics of Fluids 2016;28(4):044101.
[79] Peng DY, Robinson DB. A new two-constant equation of state. Ind Engng Chem Fundam 1976;15:59–64.
[80] Mathias PM, Naheiri M, Oh EM. A Density Correction for the Peng-Robinson Equation of State 1989;47::77–87.
[81] Péneloux A, Rauzy E, Fréze R. A consistent correction for redlich-kwong-soave volumes. Fluid Phase Equilib 1982;8(1):7–23.
[82] Bernardini F, Bajaj C. Sampling and reconstructing manifolds using alpha-shapes. Dept. Comput. Sci., Purdue Univ., West Lafayette; 1997. Technical Report CSD-TR-97-013,.
[83] Gao Q, Tao J, Hu J, Yu X. Laboratory study on the mechanical behaviours of an anisotropic shale rock. J Rock Mech Geotechn Eng 2015;7:213–9.
[84] Qu H, Pan Z, Peng Y, Zhou F. Controls on matrix permeability of shale samples from Longmaxi and Niutitang formations, China. J Nat Gas Sci Engng 2016;33: 599–610.